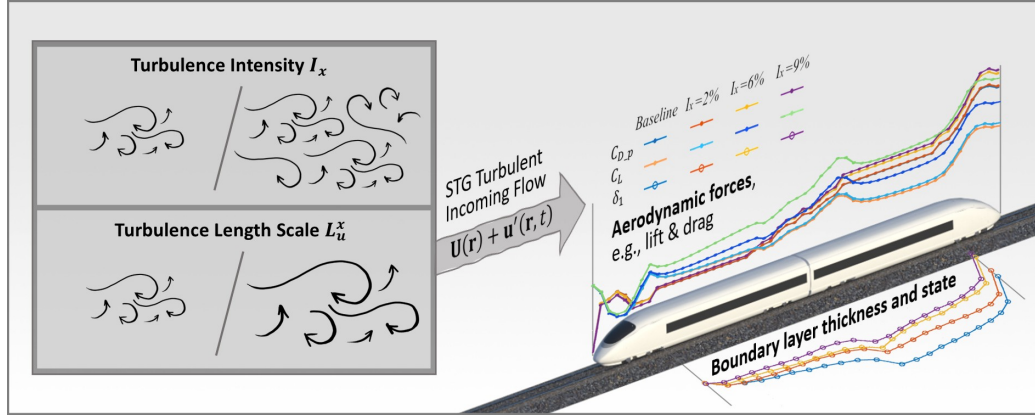


Graphical Abstract

Impact of incoming turbulence on aerodynamic forces of a high-speed train

Huanxia Wei, Chao Xia, Ting Guo, Jianyue Zhu, Zhigang Yang



Highlights

Impact of incoming turbulence on aerodynamic forces of a high-speed train

Huanxia Wei, Chao Xia, Ting Guo, Jianyue Zhu, Zhigang Yang

- Numerical simulation of high-speed trains under turbulence conditions is conducted using IDDES and STG methods.
- Both drag and lift forces increase with higher turbulence intensity.
- The impact of turbulence length scale is considered for the first time, revealing that larger incoming turbulence length scales lead to greater drag and lift forces on high-speed trains.
- The underlying mechanisms of these changes are elucidated by analyzing the flow topology in various key regions.

Impact of incoming turbulence on aerodynamic forces of a high-speed train

Huanxia Wei^a, Chao Xia^{a,b,*}, Ting Guo^a, Jianyue Zhu^c, Zhigang Yang^{a,d}

^a*School of Automotive Studies, Tongji University, Shanghai, 201804, China*

^b*Department of Mechanics and Maritime Sciences, Chalmers University of Technology, Gothenburg, 412 96, Sweden*

^c*Institute of Rail Transit, Tongji University, Shanghai, 201804, China*

^d*Beijing Aeronautical Science and Technology Research Institute, Beijing, 102211, China*

Abstract

The impact of incoming turbulence on aerodynamic characteristics of a high-speed train is numerically investigated with improved delayed detached eddy simulation (IDDES). Ten different incoming turbulence conditions are simulated by synthetic turbulence generation (STG) method. The results show that with the increase of turbulence intensity, the time-averaged drag and lift coefficients of the train rise significantly, with the maximum increase up to 46 counts and 175 counts, respectively. Moreover, the increasing rate of drag and lift coefficients grows with the turbulence length scale. The incoming turbulence produces effects analogous to those of the crosswind, reducing the impact on the head carriage while accelerating airflow around the curved sections of the tail carriage. This results in a localized drag reduction at the head and an increase at the tail. Meanwhile, the turbulent kinetic energy of the shear layer on both sides of the bogie cavity will increase with the incoming turbulence, making more flow enter the cavity and interact with the bogie and cavity, which causes the lower velocity in the underbody region and then increases the drag and lift.

Keywords: Train aerodynamics, Synthetic turbulence generation, Aerodynamic force, Unsteady effect

*Corresponding author.

Email address: chao.xia@tongji.edu.cn (Chao Xia)

1 1. Introduction

2 Research methods for aerodynamics of a high-speed train (HST) include
3 wind tunnel tests [1, 2], moving model experiments [3, 4], numerical simulations
4 [5, 6, 7], etc. In these present studies, the inlet conditions are characterized
5 by low turbulence or laminar flow. However, influenced by factors such
6 as natural winds, trackside equipment, embankments, tunnels, and viaducts,
7 the actual wind encountered on train routes is highly non-uniform. Yu et al.
8 modeled the turbulent incoming flow conditions due to natural wind during
9 the operation of HSTs, and the turbulence intensity was calculated as about
10 24.5% at the measurement point from EN 14067-6 locating at $h = 4.0m$ [8].
11 Wordley et al. found that turbulence intensity of real conditions for ground
12 vehicles ranges from 2% to 16%, or even higher, with a turbulence length
13 scale ranging from 1 to 20 meters [9]. Gao proposed that turbulent incoming
14 flow and crosswinds significantly affect the safety and economy of HSTs [10].
15 The accuracy and reliability of aerodynamic characteristics obtained from
16 numerical simulations or wind tunnel experiments can be significantly influenced
17 by inlet flow conditions that deviate from real-world environments.
18 Consequently, it is essential to investigate the effects of incoming turbulence
19 on the aerodynamic performance of HSTs to enhance the relevance and applicability
20 of research findings to actual operational conditions.

21 In the majority of research papers examining the impact of turbulence, the
22 desired turbulence components are typically introduced at the inlet through
23 experimental methods, with the research focus primarily on basic geometry
24 models. These models include square prisms [11, 12, 13, 14], Ahmed bodies
25 [15], and simplified vehicle models [16]. The turbulence generation devices
26 utilized to introduce turbulence components include passive turbulence grids
27 [11, 12, 13, 14], active grids [17], spires [16], swing mechanisms [18, 19], and
28 specialized systems [20, 21]. In addition to wind tunnel testing, recent studies
29 have utilized numerical simulations in combination with synthetic turbulence
30 generation (STG) methods to investigate the effects of turbulence, as numerical
31 methods provide improved efficiency in generating the desired turbulence
32 intensity and length scales, as well as more convenient result measurement.
33 Chen et al. investigated the impact of incoming turbulence with turbulence
34 intensity at 8.1% on wind turbine aerodynamics and wake instability using
35 improved delayed detached eddy simulation (IDDES) combined with the synthetic
36 eddy method [22], which is previously proposed by Jarrin et al [23].
37 Li et al. studied the effects of free-stream turbulence on the wind-induced

38 responses of a tall square building based on large eddy simulation (LES) with
39 discretizing and synthesizing random flow generation approach, achieving a
40 turbulence intensity of up to 28% [24]. Shur et al. proposed the synthetic
41 turbulence generator, which was validated in both canonical shear flows and
42 more complex flows with non-fixed separation points, demonstrating the sim-
43 plicity and robustness of this method [25].

44 In recent years, numerous studies have investigated the impact of tur-
45 bulence on ground vehicles. FKFS built the turbulence generation system
46 "FKFS swing" in both full-scale and 1/4 scaled automotive wind tunnels with
47 the purpose of reconstructing road turbulence conditions in testing [18, 26],
48 and later proposed a correction method for turbulent wind tunnel testing,
49 decoupling the influence of the unsteady flow from that of the static pres-
50 sure gradient in the wind tunnel [27, 19]. Based on this, they measured the
51 aerodynamic drag on various vehicle models under turbulent conditions, and
52 concluded that higher turbulence intensity increases drag. Furthermore, this
53 effect varies significantly depending on the vehicle design, highlighting the
54 importance of considering unsteady incoming conditions [28]. Cogotti et al.
55 observed that an increase in the turbulence intensity leads to a significant in-
56 crease in both the drag and the lift forces on a car in a wind tunnel, with the
57 lift increasing by 120 counts and the drag by 20-30 counts. McAuliffe et al.
58 developed the Road Turbulence System (RTS) in the 9 m NRC wind tunnel
59 with the aim of reconstructing turbulent road wind conditions in experiments
60 [21], and proved its performance compared to various other passive and ac-
61 tive turbulence generation devices [20]. This approach was used to study
62 the drag characteristics of a heavy duty vehicle (HDV) and a standard SUV,
63 revealing that the positive-drag area of HDV is larger in uniform incoming
64 flow, contrarily, that of SUV in turbulent incoming flow is larger. Gaylard et
65 al. applied the unsteady Lattice-Boltzmann method (LBM) to simulate 4%
66 and 7% turbulence intensity conditions by superimposing a three-dimensional
67 unsteady velocity field onto uniform conditions, examining the influence of
68 turbulence on a fastback saloon model. The results indicated that both drag
69 and lift increased under turbulent conditions [29]. Duncan et al. also used
70 LBM to explore the impact of turbulence on an SUV, a squareback vehicle,
71 and a notchback vehicle, demonstrating that the drag of all three models
72 increased under turbulent conditions, accompanied by changes in the shear
73 layer and wake structures, suggesting a non-linear relationship between tur-
74 bulence and its effects on vehicles [30]. Gao et al. investigated the turbulence
75 correlation between moving trains and anemometer towers, mainly focusing

on the stability under crosswind [10]. Yang et al. compared the turbulent wind characteristics over tunnel-bridge (TB) and tunnel-flat ground (TF) infrastructures for a passing HST, and proposed that the TB sites have a lower turbulence intensity about 8% due to elevated and unobstructed locations rather than TF sites, which has a higher turbulence intensity about 10% according to near-ground effect [31]. Based on Taylor's frozen turbulence hypothesis, Wu et al. analyzed the influence of the speed ratio of vehicle movement speed to the average wind speed and direction of vehicle travel on the characteristics of wind turbulence relative to moving ground vehicles, and derived the close approximation expression of the square-root coherence function of wind turbulence relative to moving ground vehicles [32].

In the present research, the aerodynamic behaviors of basic bluff bodies and simplified models have been extensively analyzed, with a focus not only on aerodynamic forces but also on wake structures and dynamics. Specifically, studies have addressed wake characteristics such as the dominant wake frequency and bi-stable switching mechanisms. For ground vehicles, the research focuses primarily on aerodynamic forces. It's generally observed that both drag and lift coefficients increase with rising turbulence intensity [29, 30, 33, 34].

However, due to the complicated geometry of HSTs, only limited investigations have explored the effects of turbulence and non-uniform wind on their aerodynamic characteristics. Common approaches involve introducing spires at the entrance of the wind tunnel, with a focus on crosswind influences [35, 36, 37, 38, 39]. Robinson et al. conducted experiments on a 1/50 scaled train model in a wind tunnel to assess the impact of turbulence [40]. Their results revealed that side force coefficients, lift force coefficients, and vortex core distributions were influenced by the interaction between vortical structures and the train wake, thereby affecting force and moment coefficients. Deng et al. reconstructed the structural wind when the HST running through a tunnel-flat ground-tunnel scenario in the wind tunnel tests with spire and the fence, and in numerical studies with IDDES as well [41, 42]. Bocciolone et al. demonstrated that turbulence has a pronounced influence on aerodynamic coefficients through comprehensive wind tunnel testing, especially at high attack angles [36]. Consistently, Cheli et al. showed that aerodynamic forces increase with turbulence intensity [37]. However, Niu et al. reported contrasting findings, observing that higher turbulence intensity led to drag reduction and a decrease in surface pressure on both the head and tail carriages of HST [43]. Xue et al. numerically investigated the

114 influence of turbulent incoming flow on an HST with a yaw angle of 90 °
115 based on IDDES, interestingly, they found that when the turbulence length
116 scale is greater than a crisis threshold of $0.5H$, load fluctuations are reduced
117 [44], and later expanded their study to wider yaw angles under turbulence
118 intensities of 5% and 20% [45]. Garca et al. conducted numerical simula-
119 tions with WMLES on HST under synthetic crosswind based on the Kaimal
120 spectrum in TurbSim with both smooth and rough train surfaces, and com-
121 pared the results of aerodynamic forces and moments [46], and then they
122 compared the results under steady wind and turbulent winds generated by
123 Kaimal spectrum (TurbSim) and Smirnov method (Ansys Fluent) [47].

124 In summary, current research on the impact of turbulence on HSTs has
125 primarily focused on aerodynamic forces. Due to the lack of detailed flow field
126 data and pressure distribution information, the mechanism though which
127 turbulence affects aerodynamics remains unclear, and conclusions are incon-
128 sistent. Furthermore, previous studies have largely overlooked the effects
129 of turbulence length scales. The primary objective of this paper is to ad-
130 dress these gaps by investigating the influence of both turbulence intensity
131 and turbulence length scales on the aerodynamic characteristics of HSTs. In
132 addition to aerodynamic forces, flow field details such as surface pressure
133 distribution and boundary layer formation and development are analyzed to
134 provide deeper insights into the underlying mechanisms.

135 The remainder of this paper is structured as follows. Section 2 introduces
136 the setup of the numerical simulation cases, including the geometric models,
137 numerical methods, as well as the initial and boundary conditions. Addition-
138 ally, the methods for synthetic turbulence generation and turbulence repre-
139 sentations are briefly described. Section 3 focuses on the impact of varying
140 turbulence intensity and length scale on aerodynamic forces, boundary layer
141 characteristics, and surface pressure distributions, providing a detailed dis-
142 cussion of the underlying mechanisms and the potential link between them.
143 Finally, the conclusions are summarized in Section 4.

144 2. Methods

145 2.1. Geometry and computational domain

146 A 1/18 scaled CRH3 HST model with two carriages is used in the sim-
147 ulation (Figure 1). The model measures 2.894 m in length (L) \times 0.183 m
148 in width (W) \times 0.201 m in height (H). In addition to four bogies and bo-

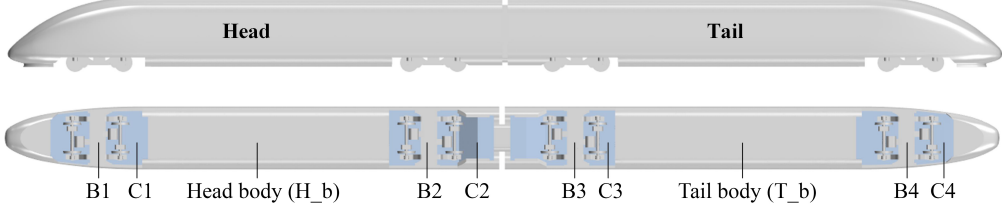


Figure 1: Geometry of 1/18 scaled CRH3 HST model. C represents the bogie cavity, and B represents the bogie. H_b and T_b are head body and tail body, respectively. These abbreviations are to be referred hereunder.

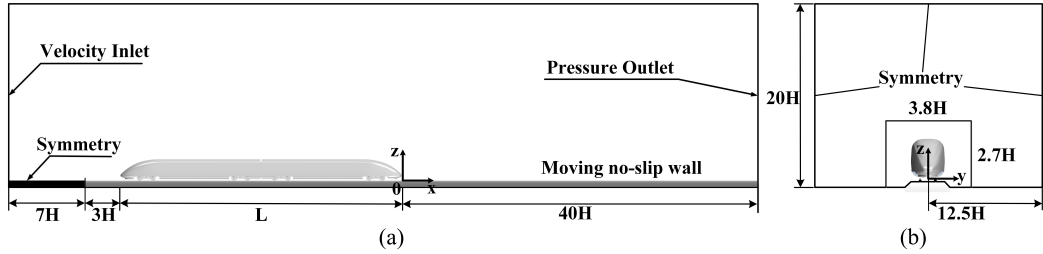


Figure 2: Computational domain and boundary conditions. The coordinate system (x , y , z) is superposed, with the origin located at the top of the rail. The small rectangle with width of $3.8H$ in (b) indicates the STG region.

149 gie cavities, two cowcatchers and one intercarriage junction gap (hereinafter
150 referred to as "carriage junction") are also included.

151 As shown in Figure 2, the dimensions of the computational domain are
152 $64.4H \times 25H \times 20H$ (length \times width \times height), where H represents the
153 height of the HST model. In the underbody region of the HST, a 1/18
154 single track ballast and rail (STBR) ground configuration is implemented,
155 in accordance with the Technical Specifications for Interoperability (TSI)
156 standard [48]. The boundary conditions are set as follows: a velocity inlet
157 and pressure outlet, a non-slip wall condition for the train body, a slip wall
158 with a matching the inlet velocity for the STBR and ground, and slip walls
159 for the others boundaries. The free stream velocity U_∞ is 58 m/s, resulting
160 in a Reynolds number of 7.2×10^5 , based on U_∞ and the carriage width W .

161 To investigate the influence of incoming turbulence, various turbulence
162 intensities and length scales are introduced at the inlet using synthetic tur-
163 bulence generation (STG), which is applied in the region where the mesh size
164 is relatively uniform, as indicated by the small rectangle in Figure 2b.

165 *2.2. Numerical method*

166 The improved delayed detached eddy simulation (IDDES), based on $k-\omega$
 167 SST, is employed for the numerical study. Proposed by Shur et al.[49], ID-
 168 DES combines the advantages of delayed detached eddy simulation (DDES)
 169 and wall-modeled large eddy simulation (WMLES), and will activate RANS
 170 and LES in different regions to obtain a satisfactory balance between compu-
 171 tational accuracy and computational resource consumption. In our previous
 172 studies, the same model was used, with detailed descriptions of the numerical
 173 method provided in [5, 50, 51].

174 In this study, to achieve satisfactory reliability and numerical accuracy,
 175 the domain is discretized using Poly-Hexcore mesh, which automatically con-
 176 nects the prism layers to the hexahedral mesh regions. Three mesh sets with
 177 different refinement levels (coarse, medium, and fine) are used in the conver-
 178 gence check to demonstrate mesh independence, consisting of 23.3, 38.5, and
 179 50.6 million cells, respectively. The primary differences among these grids
 180 lie in the spatial resolution on the surface and in the wake region, as listed
 181 in Table 1. The near-wall boundary layers for them remain consistent, each
 182 containing 20 extruded cells with $y^+ \leq 1$ and a total height of 0.03H. The
 183 mesh at the medium refinement level around the train with details is shown
 184 in Figure 3.

Table 1: Spatial resolution details for mesh of the train, bogie, and wake region.

Refinement level	Train surface	Bogie surface	Wake region	Total mesh number
Coarse	0.01 - 0.03 H	0.01 - 0.015 H	0.03 H	23.3 million
Medium	0.005 - 0.02 H	0.005 - 0.01 H	0.02 H	38.5 million
Fine	0.005 - 0.015 H	0.005 - 0.01 H	0.018 H	50.6 million

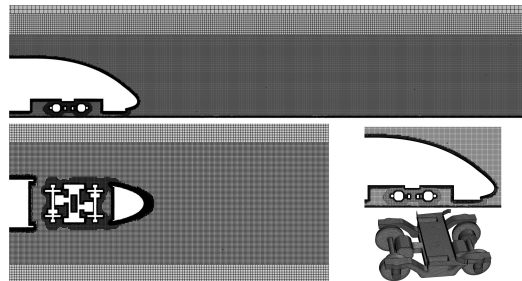


Figure 3: Mesh distribution around a HST at medium refinement level.

185 *2.3. Mesh convergence and numerical validation*

186 To ensure the numerical reliability of the simulations, a series of mesh
 187 convergence check was conducted to verify the mesh independence. Subse-
 188 quently, the numerical results were validated against the wind tunnel data
 189 to confirm their accuracy.

190 For the mesh convergence study, force coefficients are treated as conver-
 191 gence criteria, and defined by Eq. 1-3, where C_D , C_{Dp} , C_{Dv} , C_L and C_S
 192 are the drag coefficient, pressure drag coefficient, viscous drag coefficient, lift
 193 coefficient, and side force coefficient, respectively.

$$194 \quad C_D = \frac{F_x}{\frac{1}{2}\rho U_\infty^2 A_x}, C_{Dp} = \frac{F_{xp}}{\frac{1}{2}\rho U_\infty^2 A_x}, C_{Dv} = \frac{F_{xv}}{\frac{1}{2}\rho U_\infty^2 A_x} \quad (1)$$

$$195 \quad C_L = \frac{F_z}{\frac{1}{2}\rho U_\infty^2 A_x} \quad (2)$$

$$196 \quad C_S = \frac{F_y}{\frac{1}{2}\rho U_\infty^2 A_x} \quad (3)$$

197 where F_x , F_{xp} , F_{xv} , F_y and F_z are the total drag, pressure drag, viscous
 198 drag, side force and lift force, respectively. Additionally, ρ is the density of
 199 the air, U_∞ is the free stream velocity, and A_x is the projected area in the
 200 streamwise direction. The pressure coefficient C_P is defined in Eq. 4, where
 201 P is the time-averaged surface pressure and P_∞ is the static pressure of the
 202 incoming flow.

$$203 \quad C_P = \frac{P - P_\infty}{\frac{1}{2}\rho U_\infty^2} \quad (4)$$

204 For numerical validation, the simulation under stationary ground condi-
 205 tions for the train with three carriages is compared against the wind tunnel
 206 tests conducted at the Shanghai Automotive Wind Tunnel Center (SAWTC).
 207 This validation includes aerodynamic forces and pressure measurements. The
 208 Reynolds number for the wind tunnel test is 7.20×10^5 , consistent with the
 209 numerical simulation. The HST model used in the wind tunnel test is at
 210 a 1/8 scale and retains the detailed crescent-shaped structures and air con-
 211 ditioning fairings, which are simplified in the numerical simulation. More
 212 detailed information regarding the wind tunnel tests was provided in our
 213 previous study [50].

212 Figure 4a shows the time-averaged C_D for the head carriage, tail carriage,
 213 and the entire train set across the three refinement levels, alongside the wind
 214 tunnel tests. The numerical results for all cases show good agreement. For
 215 the three different mesh refinement levels, the deviation in C_D among the
 216 meshes is less than 1%. Compared with the wind tunnel data, the deviation
 217 in C_D for both head and tail carriage in the IDDES (medium refinement) is
 218 less than 5%. For C_L (Figure 4b), the deviation among the three meshes is
 219 less than 7%, and between the medium and fine mesh is within 4%.

220 Figure 5 presents the distribution of C_P along the longitudinal symmetry
 221 line of the upper surface for the head and tail carriages, comparing the nu-
 222 matical results from three meshes levels with the wind tunnel tests. For the
 223 mesh convergence, the results for the three refinement levels are generally

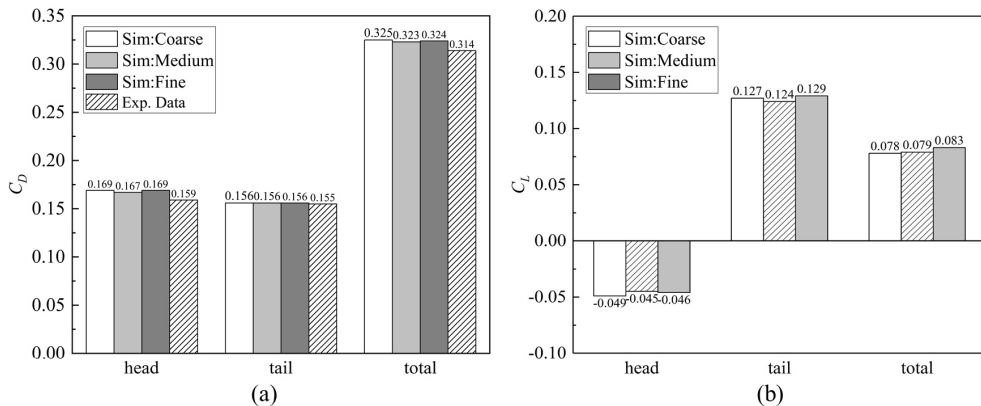


Figure 4: Time-averaged force coefficients of the head carriage, tail carriage and total train set based on coarse, medium and fine mesh and wind tunnel tests: (a) C_D and (b) C_L .

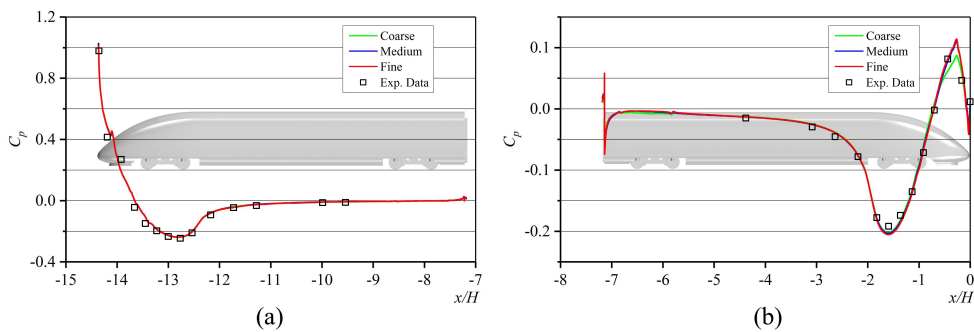


Figure 5: Time-averaged C_P of the longitudinal symmetry line based on coarse, medium and fine mesh and wind tunnel tests: (a) the head carriage; (b) the tail carriage.

224 in good agreement, with minor discrepancies observed for the coarse mesh,
 225 particularly at the nose edge of the tail carriage. The pressure distribution
 226 from the IDDES with medium mesh level also demonstrates good agreement
 227 with the experimental results.

228 Overall, considering the balance between computational cost and accu-
 229 racy, subsequent simulations are conducted using the medium mesh. The
 230 results from this mesh show satisfactory mesh independence and are well-
 231 aligned with the wind tunnel data in terms of aerodynamic forces and pres-
 232 sure distribution.

233 *2.4. Turbulence representations and generation*

234 Turbulence measures focused in this study include turbulence intensity
 235 and turbulence length scale. Turbulence intensity is an critical parameter to
 236 represent the level of turbulence in the wind, defined as the ratio of velocity
 237 fluctuations to the mean velocity [52]. Accordingly, the turbulence intensity
 238 in three directions is expressed as follows:

$$I_x = \frac{U_{rms}}{U_\infty}, \quad I_y = \frac{V_{rms}}{U_\infty}, \quad I_z = \frac{W_{rms}}{U_\infty}, \quad (5)$$

239 where I_x , I_y , and I_z are the longitudinal, lateral, and vertical turbulence
 240 intensity, respectively, and U_{rms} , V_{rms} , and W_{rms} denote the velocity fluctua-
 241 tions in the corresponding directions.

242 Regarding turbulence length scales, two common calculation methods are
 243 the autocorrelation method [53] and the Von Karman spectral fitting method
 244 [54]. The autocorrelation method provides an estimate of the average vortex
 245 size in a turbulent wind field, and value by the Von Karman spectral fitting
 246 method is generally half of that by the autocorrelation method [9]. In this
 247 paper, the autocorrelation method is used to determine the turbulence length
 248 scale.

249 There are nine turbulent length scales corresponding to the three direc-
 250 tions related to the longitudinal, lateral, and vertical fluctuating velocity
 251 components, i.e., u , v , and w . For example, L_u^x , L_u^y , and L_u^z denote the av-
 252 erage size of vortices in the x , y , and z directions related to the longitudinal
 253 fluctuating velocity components, respectively. They are defined as:

$$L_u = \frac{1}{\sigma_u^2} \int_0^\infty R_{12}(x) dx, \quad (6)$$

254 where $R_{12}(x)$ is the cross-correlation function of the longitudinal fluctuating
 255 velocities, i.e., $u_1 = u(x_1, y_1, z_1, t)$ and $u_2 = u(x_1+x, y_1, z_1, t)$, at two different
 256 x positions, and σ_u is the variance of the longitudinal fluctuating velocity u .
 257 According to the Taylor hypothesis, if the vortex moves at the average wind
 258 speed U , the fluctuating velocity $u(x_1, t+\tau)$ can be expressed as $u(x_1 - x, \tau)$,
 259 where $x = U\tau$. Therefore, Eq. 6 can be further expressed as:

$$L_u^x = \frac{U}{\sigma_u^2} \int_0^\infty R_u(\tau) d\tau, \quad (7)$$

260 where $R_u(\tau)$ is the autocorrelation function of the fluctuating velocity $u(x_1, t+\tau)$. L_u^y and L_u^z are calculated similarly.
 261

262 In addition to the turbulence representations, the turbulence generation
 263 method in numerical studies is described. To impose specific turbulence
 264 conditions at the inlet, the STG method is employed in this study. The
 265 STG method generates time-dependent inlet conditions by superimposing
 266 a vector of synthetic velocity fluctuations onto the initial steady velocity
 267 field. Consequently, the velocity vector at a point $\mathbf{r} = \{x, y, z\}$ of an inlet
 268 boundary condition is specified as:

$$\mathbf{U}(\mathbf{r}, t) = \mathbf{U}_{\text{Inlet, mean}}(\mathbf{r}) + \mathbf{u}'(\mathbf{r}, t), \quad (8)$$

269 where $\mathbf{U}_{\text{Inlet, mean}}(\mathbf{r})$ is the mean velocity vector at the inlet, and $\mathbf{u}'(\mathbf{r}, t)$
 270 is the vector of synthetic velocity fluctuations. More detailed information
 271 regarding the STG method and the definitions of symbols can be found in
 272 the reference [25].

273 2.5. Inflow turbulence conditions

274 To investigate the impact of inflow turbulence, ten cases with varying
 275 inflow turbulence conditions are simulated, with turbulence intensity ranging
 276 from 2% to 9% and turbulence length scale from 0.37H to 1.04H. The details
 277 of the inflow turbulence conditions for each case are listed in Table 2. The
 278 first case serves as the Baseline, featuring a uniform inflow inlet without using
 279 the STG method. The turbulence intensity and turbulence length scale in
 280 the table are calculated at the reference point, marked red in Figure 6. The
 281 reference point is located as close as possible to the train's front to accurately
 282 represent the actual turbulent inlet conditions, while maintaining sufficient
 283 distance to avoid interference from the train. The height of the point is

Table 2: The inflow turbulent conditions for the ten numerical cases.

No.	Case name	Turb. intensity I_x	Turb. length scale L_u^x
1	Baseline	—	—
2	Ix02_L040H	2%	0.40H
3	Ix02_L051H	2%	0.51H
4	Ix02_L100H	2%	1.00H
5	Ix04_L038H	4%	0.38H
6	Ix06_L104H	6%	1.04H
7	Ix07_L038H	7%	0.38H
8	Ix09_L056H	9%	0.56H
9	Ix09_L091H	9%	0.91H
10	Ix09_L037H	9%	0.37H

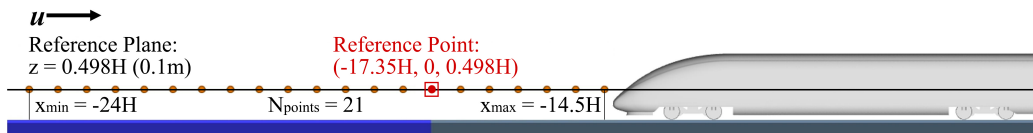


Figure 6: The location of the reference plane and points on the symmetry plane.

284 sufficient to minimize ground effects, with its selection based on trends in
285 both longitudinal and vertical turbulence values.

286 Figure 7 shows the turbulence intensity and length scale of selected cases,
287 measured at the 21 reference points marked in Figure 6, distributing along
288 the flow direction on the middle plane. The imposed turbulence intensity
289 and length scale at the inlet are observed to decay at different rates as the
290 flow moves downstream, particularly in cases with high turbulence intensity.
291 Then subsequent flow field comparison results demonstrate the direct impact
292 of the turbulent conditions on the flow surrounding the HST.

293 Figure 8 presents the instantaneous velocity distribution on the plane
294 $z = 0.175H$. It can be observed that for low turbulence intensity (2%,
295 Figure 8b), the changes in the velocity field are not significant, though the
296 introduction of turbulence components can still be seen. As the turbulence
297 intensity further increases (9%, Figure 8c-d), noticeable velocity fluctuations
298 are introduced into the flow domain by STG, resulting in increased non-
299 uniformity. Additionally, the change in turbulence length scale is clearly
300 reflected, with larger turbulence length scales leading to larger vortex struc-

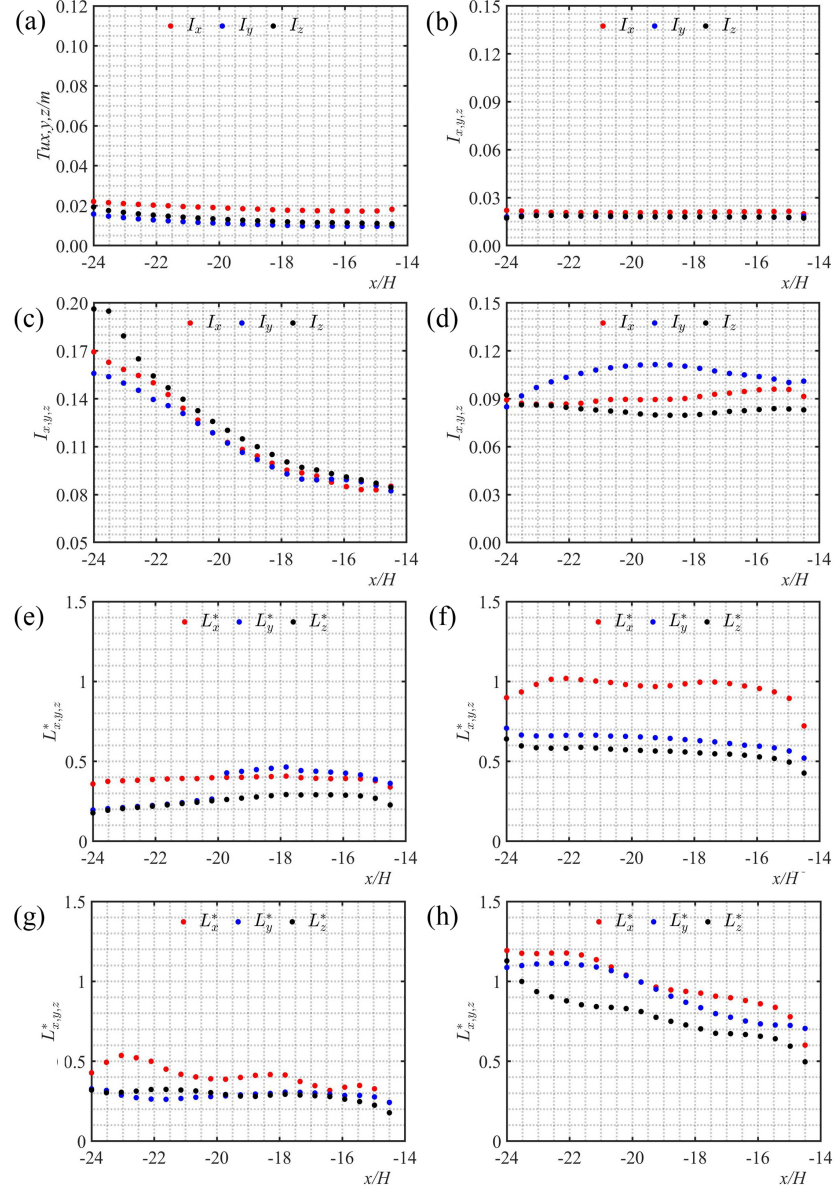


Figure 7: The calculation results of turbulence intensity and turbulence length scale along the flow direction at the longitudinal symmetry line of 0.1m height from the origin are as follows: varying turbulence intensity: (a) Ix02_L040H; (b) Ix02_L100H; (c) Ix09_L037H; (d) Ix09_L091H; varying turbulence length scale: (e) Ix02_L040H; (f) Ix02_L100H; (g) Ix09_L037H; (h) Ix09_L091H.

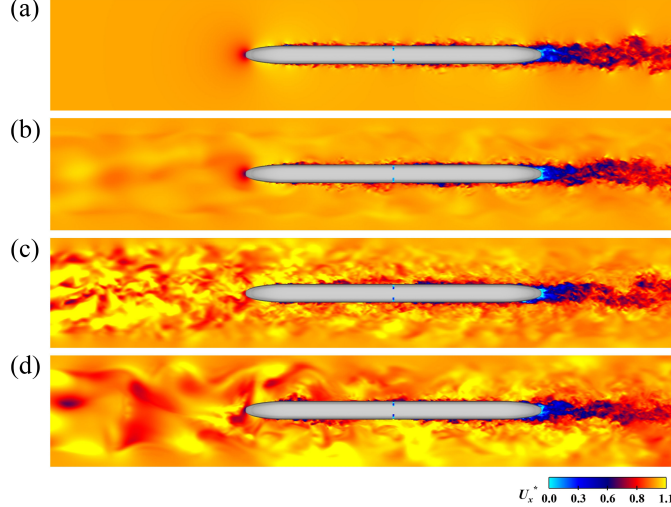


Figure 8: The instantaneous velocity distribution of plane $z=0.175H$: (a) Baseline; (b) Ix02_L100H; (c) Ix09_L037H; (d) Ix09_L091H.

tures, particularly upstream of the HST. These observations demonstrate the effectiveness, accuracy, and controllability of the STG method in introducing turbulence for the numerical cases presented in this study.

3. Results and discussion

In this section, the influence of two key turbulence representative parameters, turbulent intensity (Section 3.1) and length scale (Section 3.2), on the aerodynamic characteristics of HSTs in operation are separately presented and discussed. For each of them, the changes in aerodynamic forces, boundary layer characteristics, and pressure distribution are examined in detail.

3.1. Turbulence intensity

3.1.1. Aerodynamic forces

The analysis of aerodynamic forces begins with the time-averaged integral force coefficients, changing along with turbulence intensity at different length scales, shown in Figure 9. Trends in drag and lift coefficients at three turbulence length scales ($L_u^x \approx 0.4H$, $L_u^x \approx 0.6H$, $L_u^x \approx 1.0H$, marked in different labels) are studied in groups.

First, and most obviously, the drag and lift coefficients show an increasing trend with increasing turbulence intensity at all turbulence length scales.

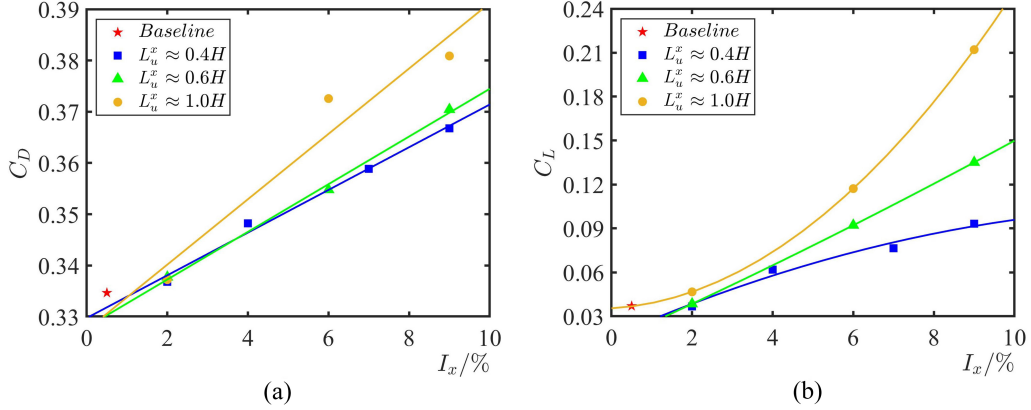


Figure 9: Distribution of time-averaged integral force coefficients with turbulence intensity: (a) drag coefficient (C_D); (b) lift coefficient (C_L).

319 For the drag coefficient, its increase is more linear, and the growth rate is
 320 higher at larger turbulence length scales ($L_u^x \approx 1.0H$). Specifically, The
 321 larger deviation of the drag coefficient from the regression line at $I_x = 6\%$
 322 and $I_x = 9\%$ is due to the larger turbulence length scale than 1.0H of $I_x = 6\%$
 323 (1.04H) and smaller of the latter (0.91H). However, for the lift coefficient, the
 324 growth rate with turbulence intensity is not still constant, and influenced by
 325 the turbulence length scale. When the turbulence length scale is relatively
 326 small ($L_u^x < 0.6H$), its trend exhibits a sub-linear pattern, whereas under
 327 large-scale conditions ($L_u^x > 0.6H$), it displays a super-linear behavior. This
 328 difference indicates that the turbulence length scale has a more pronounced
 329 effect on lift rather than drag. As turbulence intensity has a more significant
 330 impact at the large turbulence length scale ($L_u^x \approx 1.0H$), we focus our fol-
 331 lowing analysis on this scale, i.e., case 4 (Ix02_L100H), case 6 (Ix06_L104H),
 332 and case 9 (Ix09_L091H).

333 To better understand the mechanisms through how turbulence intensity
 334 influences the aerodynamic forces on the train, it is essential to examine indi-
 335 vidual carriages separately. Therefore, the following analysis focuses on the
 336 aerodynamic force trends for both the head and tail carriages under varying
 337 turbulence intensities, aiming to determine which carriage primarily con-
 338 tributes to the overall aerodynamic response to turbulence intensity. Figure
 339 10 illustrates the changes in aerodynamic coefficients relative to the Baseline
 340 of two carriages respectively, under three various turbulence intensity con-
 341 ditions. The results of time-averaged drag coefficient (Figure 10a) indicate

that, the drag by both the head carriage and the tail carriage increase as turbulence intensity rises. Compared with the Baseline, the drag increase for the tail carriage is higher than that for the head carriage. Under low turbulence intensity ($I_x = 2\%$), the drag increment remains minimal, whereas at high turbulence intensity ($I_x = 9\%$), the total drag coefficient increases by 46 counts (+14%). When under $I_x = 6\%$, this trend of increasing drag has already become distinct, with the total drag coefficient increasing by 38 counts (+11%).

On the other hand, regarding the time-averaged lift coefficient (Figure 10b), turbulence intensity shows a more significant impact on lift than on drag, aligning with previous results of the entire train set. At low turbulence intensity, similar to the drag results, the lift increment is minor, however, at medium and high turbulence intensities, the total lift coefficient increases by factors of 2.2 and 4.7, respectively. Notably, unlike the drag results,

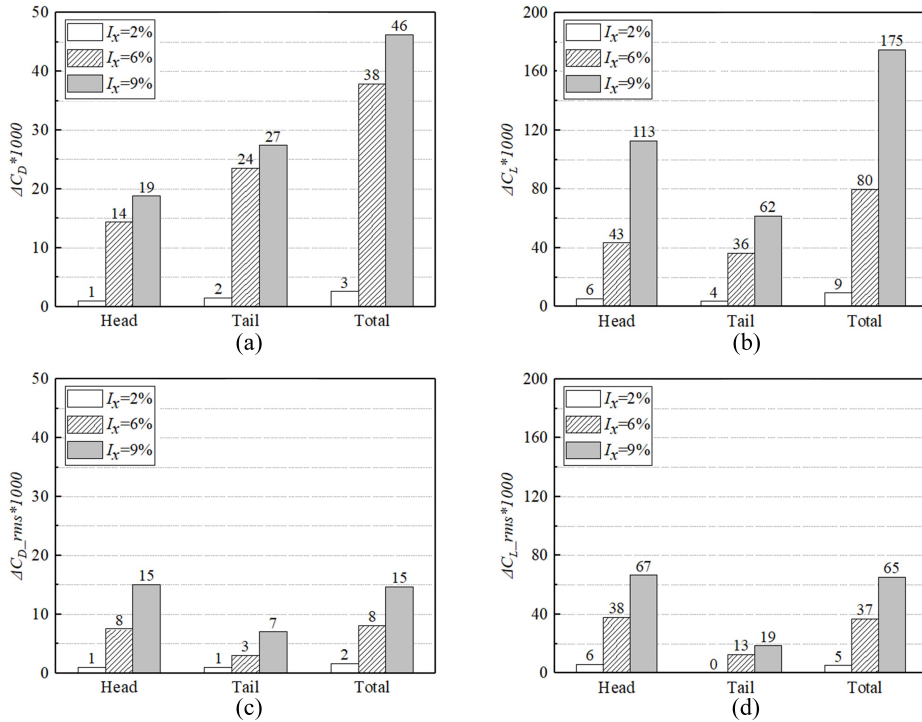


Figure 10: The increment of aerodynamic force coefficients of the two carriages at large turbulence length scale under different turbulence intensities: (a) time-averaged C_D ; (b) time-averaged C_L ; (c) RMS of C_D ; (d) RMS of C_L .

turbulence intensity exerts a more substantial effect on the lift of the head carriage than on the tail carriage.

Furthermore, Figure 10c-d presents the increments in the root mean square (RMS) of the drag and lift coefficients, representing the fluctuation levels of aerodynamic forces. Both the RMS of drag and lift increase with rising turbulence intensity, with the head carriage exhibiting a greater increase than the tail carriage. As expected, under high turbulence intensity conditions, alternating loads are exerted on the carriage surface, leading to stronger fluctuations in aerodynamic forces, and might further affect the HST operating smoothness when facing the turbulent wind.

To further investigate the variation of aerodynamic forces for each component of the train separately, especially for bogie structures, the increment of aerodynamic force coefficients of more train components are obtained and shown in Figure 11. Figure 11a shows that with the increase of turbulence intensity, the C_D of the head carriage mainly increases in the first bogie cavity (C_1) and the second bogie (B_2), while that of the head body did not change significantly. The C_D of all components of the tail carriage increased along with turbulence intensity, with the largest increase observed in the tail body. Interestingly, for most of the components of the tail carriage, especially the

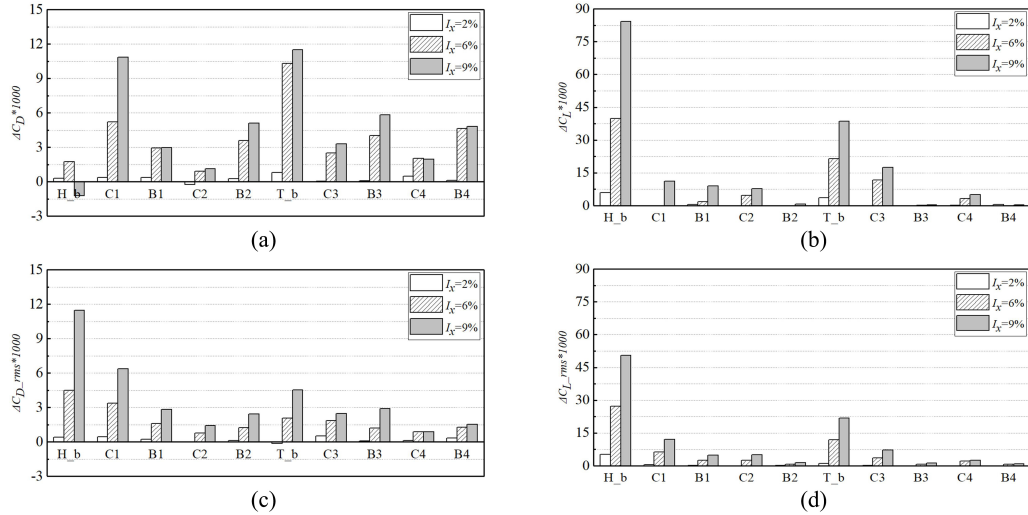


Figure 11: The increment of aerodynamic force coefficients of train components at large turbulence length scale: (a) time-averaged C_D ; (b) time-averaged C_L ; (c) RMS of C_D ; (d) RMS of C_L . The representing train components of abbreviations C_1 , B_1 , C_2 , B_2 , C_3 , B_3 , C_4 , B_4 are given in Figure 1.

375 fourth bogie region (including bogie and cavity), the drag-increasing effect of
376 the turbulence intensity occurs mainly before $I_x = 6\%$, while further increasing
377 the turbulence intensity does not result in a significant drag change. As
378 for C_L (Figure 11b), with the increase of turbulence intensity, the C_L of the
379 head body increases significantly, followed by the tail body. In addition, the
380 third bogie cavity has shown its distinct contribution to the increase in lift.
381 For the RMS of C_D and C_L (Figure 11c-d), the main contributing regions
382 of increase in drag fluctuations are the head body and first bogie cavity C_1 ,
383 which are close to trend of lift fluctuation is basically similar to that of drag.

384 To clarify the mechanism with respect to the increase in aerodynamic
385 drag, it is further decomposed into pressure drag and viscous drag. Their
386 development on the head body along the flow direction is shown in Figure 12,
387 including the absolute values (solid lines, left axis) and their variance from
388 Baseline (dashed lines, right axis).

389 The development of pressure drag is first focused on, shown in Figure 12a.
390 From its absolute values along the flow direction of Baseline, it is obvious
391 that, the contributions of the three non-smooth regions to the pressure resis-
392 tance are essentially equal. In other words, each of nose and bogie structure
393 of head carriage, them of tail carriage, and carriage junction region, con-
394 tributes approximately 0.08 in pressure drag coefficient. As for the impact of
395 turbulence conditions, when the turbulence intensity is low ($I_x = 2\%$), there
396 is only a slight variance, while as it becomes greater, influence on pressure
397 drag is significant. Among these changes in C_D , when the turbulence in-
398 tensity increases from 2% to 6%, the main contribution region starts behind
399 the second bogie structure. On the one hand, it is worth noting that, the
400 variance in cumulative pressure drag rises very quickly at the non-smooth
401 carriage junction and the third bogie region. On the other hand, the rear
402 region ($x > -2H$) also shows a great influence, where the flow detachment
403 occurs and the wake starts development.

404 Further increasing the turbulence intensity to 9% does not produce such
405 a large variance, during which, this variance is mainly due to the carriage
406 junction and the third bogie structures. Although the values of the two are
407 also separated at the front of the carriage ($x < -12H$), the effects of the
408 drag-enhancing and drag-reducing regions counteract each other. Finally,
409 the cumulative pressure drag of $I_x = 6\%$ and $I_x = 9\%$ becomes the same at
410 the straight section of the head carriage. It is concluded that the structure
411 of the carriage junction has a very strong influence on the aerodynamic drag
412 under high turbulence intensity conditions ($I_x \geq 6\%$) compared to other com-

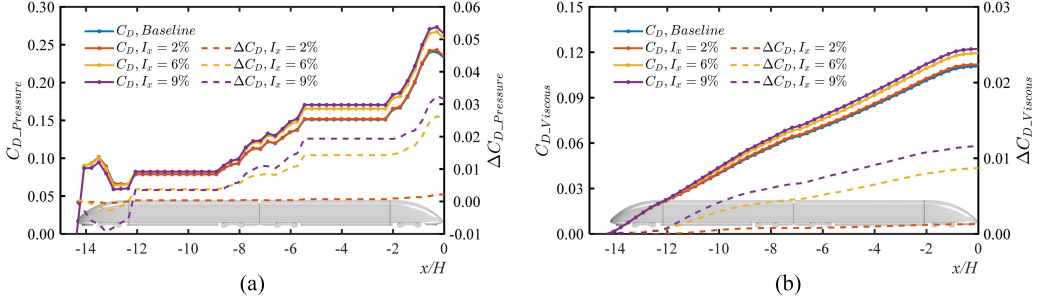


Figure 12: Decomposed cumulative drag coefficients along the flow direction at large turbulence length scale of $L_u^x \approx 1.0H$ under varying turbulence intensity: (a) pressure drag $C_{D_Pressure}$; (b) viscous drag $C_{D_Viscous}$.

413 ponents. In order to better reduce the drag increasing under wind conditions
 414 with large turbulence intensity, it is crucial to smoothly connect neighboring
 415 carriages, or to use active or passive flow control approaches for aerodynamic
 416 drag reduction in this region.

417 Figure 12b shows the development of viscous drag coefficient. From the
 418 absolute values, it is obvious that viscous drag consistently rises along the
 419 flow direction due to the skin friction. Case under $I_x = 2\%$ continues to
 420 exhibit similarly to Baseline, with an insignificant increase in viscous drag.
 421 As the turbulence intensity increases from 2% to 6%, the difference presents
 422 from $x = -12H$, and then grows linearly along the flow direction. The
 423 effect of further increasing the turbulence intensity is concentrated in the
 424 straight section of the head carriage, which might attribute to changes in the
 425 boundary layer state.

426 Figure 13 shows the lift coefficient development along the flow direction
 427 at large turbulence length scale ($L_u^x \approx 1.0H$). First, negative lift (downforce)
 428 is generated at the windward curve section (front edge) of the head carriage,
 429 while the curve section of the tail carriage generates a significant increase
 430 in lift, which is in line with expectations. In addition, the lift is generally
 431 increased in the bogie regions, especially in the first and third bogie regions.
 432 At the same time, the straight sections of the carriage reduce the lift, and
 433 the reduction is the fastest when the air is just entering the straight section.

434 Similar to drag, the influence of turbulence intensity on lift is discussed.
 435 It is clear that when the turbulence intensity increases, lift in basically all
 436 regions shows an increase. For $I_x = 2\%$, the increase is not significant, while
 437 further increases have a significant influence. For Baseline and $I_x = 2\%$, lift

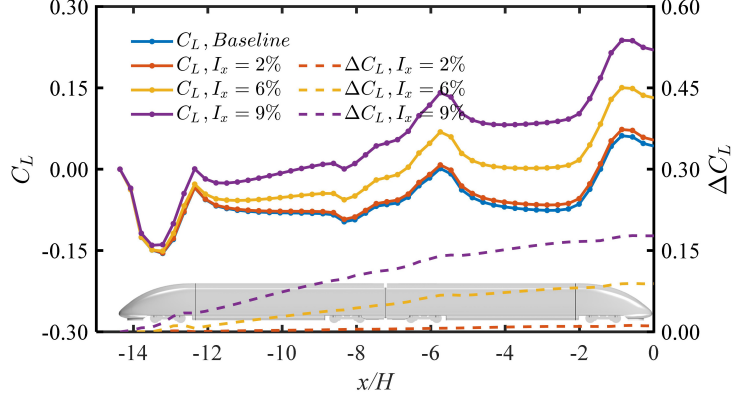


Figure 13: Cumulative lift coefficients along the flow direction at large turbulence length scale of $L_u^x \approx 1.0H$ under varying turbulence intensity.

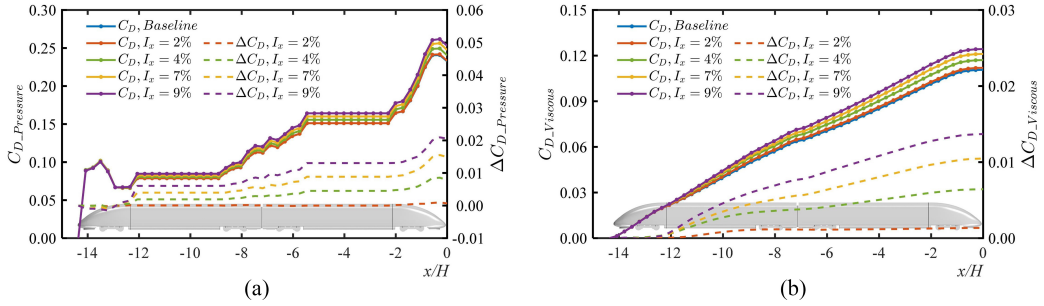


Figure 14: Decomposed cumulative drag coefficients along the flow direction at small turbulence length scale of $L_u^x \approx 0.40H$ under varying turbulence intensity: (a) pressure drag $C_{D_Pressure}$; (b) viscous drag $C_{D_Viscous}$.

is negative in all regions, except for the rear edge of the tail carriage. As for higher turbulence intensity, the cumulative drag is always positive after passing through the first bogie region. More importantly, the final total lift coefficients show a huge difference, with the lift coefficient in high turbulence intensity condition ($I_x = 9\%$) exceeding the Baseline by even more than four times, and more than twice as high in moderate turbulence intensity ($I_x = 6\%$), leading to the same conclusion as shown in Figure 9. A certain increase in lift force is beneficial for reducing energy consumption and increasing rail life. Therefore, the results show that traditional experimental and numerical studies under low turbulence intensity conditions may be biased to estimate these performance of HST.

The above analysis and discussion are all based on the conditions under

450 large turbulence length scale ($L_u^x \approx 1.0H$). Therefore, Figure 14 depicts the
 451 decomposed drag under smaller turbulence length scale ($L_u^x \approx 0.40H$). The
 452 overall trends under different turbulence intensities are similar to those at a
 453 large turbulence length scale as discussed before. However, the influence of
 454 turbulence intensity is notably weaker at the small turbulence length scale.

455 *3.1.2. Boundary layer*

456 From the previous discussion in Section 3.1.1, it is observed that the
 457 viscous drag increases with higher turbulence intensity. In order to further
 458 study the formation mechanism of viscous drag, the boundary layer is stud-
 459 ied, whose formation and development directly determine the magnitude and
 460 distribution of viscous drag exerted on the train surface. To quantitatively
 461 study the boundary layer, the displacement thickness δ_1 , momentum thick-
 462 ness δ_2 and shape factor H_{12} are introduced, which are defined as:

$$463 \quad \delta_1 = \int_0^\infty \left(1 - \frac{u}{U_\infty}\right) dy; \quad (9)$$

$$464 \quad \delta_2 = \int_0^\infty \frac{u}{U_\infty} \left(1 - \frac{u}{U_\infty}\right) dy; \quad (10)$$

$$465 \quad H_{12} = \frac{\delta_1}{\delta_2}, \quad (11)$$

466 where u is the time-averaged velocity at a given point in the boundary layer,
 467 and U_∞ is the free-stream velocity outside the boundary layer. Among them,
 468 δ_1 describes the equivalent wall offset distance that represents the blockage
 469 effect of the boundary layer on fluid volumetric flow rate, while δ_2 focuses on
 470 the equivalent wall offset distance for momentum loss caused by boundary
 471 layer. The quotient of them two (H_{12}) represents the fullness of the bound-
 472 ary layer velocity profile, and lower H_{12} means a fuller velocity profile and
 473 larger the velocity gradient. Generally high H_{12} indicates a laminar bound-
 474 ary layer, with a relatively low viscous drag, while low H_{12} is obtained for
 475 turbulent boundary layer. Figure 15 shows the displacement thickness δ_1 and
 476 momentum thickness δ_2 along the longitudinal symmetry line at the top of
 the train.

477 It can be observed that both the displacement thickness δ_1 and momen-
 478 tum thickness δ_2 of the boundary layer increase along the flow direction, indi-
 479 cating a typical development of boundary layer. However, at the rear side of

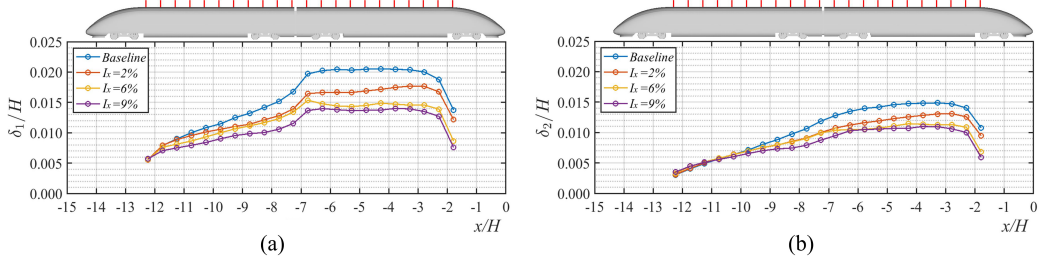


Figure 15: Displacement thickness and moment thickness along the longitudinal symmetry line at the top of the train under varying turbulence intensity: (a) displacement thickness δ_1 ; (b) moment thickness δ_2 .

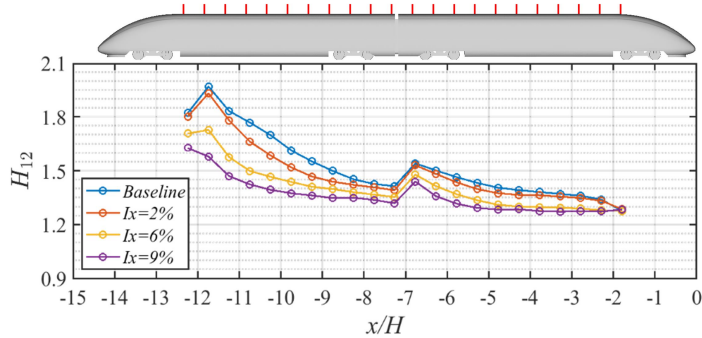


Figure 16: Shape factor H_{12} along the longitudinal symmetry line at the top of the train under varying turbulence intensity.

the tail carriage before entering the curve section, the boundary layer thickness decreases, likely due to the contraction effect induced by the streamlined tail on the surrounding flow. In this region, a decrease in pressure and an increase in flow velocity occur, resulting in reduced momentum exchange, which ultimately suppresses and reverses the further development of the boundary layer. In addition, comparing the two thickness indicators, it is shown that δ_1 tends to stop changing in the straight section of the tail carriage, while δ_2 is still slowly increasing. Therefore, after the development stage of the boundary layer of the head carriage and the later disturbance of the carriage junction region, the volume of fluid included in the boundary layer has basically not changed. However, at the same time, momentum exchange between inside and outside the boundary layer continues to occur, hence the boundary layer tends to a more turbulent state. As for the impact of turbulence intensity, the final thickness of the boundary layer is essentially the same

under different turbulence intensities. Although, a higher turbulent intensity leads to thinner initial and developing boundary layer.

The shape factors are shown in Figure 16. The shape factor is decreasing along the flow direction, indicating that the flow state within the boundary layer continuously tends to turbulence as the boundary layer develops. At the junction of the two carriages, the separation and reattachment of the airflow temporarily reverse the development of the boundary layer. In addition, it is obvious that the shape factor decreases as the turbulence intensity increases, representing a higher velocity gradient under high turbulence intensity, which leads to higher viscous drag comparing to low turbulence conditions.

3.1.3. Pressure distribution

The surface pressure distribution of HST, which is also affected by the incoming turbulence, can be used to locate the source of pressure drag, and provide valuable insights for studies of the wind load of the carriage and train aeroacoustics.

Figure 17 shows the front view of the time-averaged surface pressure coefficient on the head carriage under Baseline and two turbulence conditions ($I_x = 2\%$ and $I_x = 9\%$). For clearly presenting the differences, the raw value is used for the baseline, and the surface distributions of the pressure difference compared with the Baseline are calculated for turbulence cases. The surface pressure coefficient difference between the turbulence cases and the Baseline is defined as:

$$\Delta C_{P(2\%)} = C_P|_{I_x=2\%} - C_P|_{\text{Baseline}}, \quad (6)$$

where $\Delta C_{P(2\%)}$ is the pressure difference between $I_x = 2\%$ and the Baseline. The pressure difference under other conditions is defined in the same way.

For the low turbulence intensity case ($I_x = 2\%$), the surface pressure on the front of the head carriage shows minimal variation compared to the Baseline, resulting in only a slight difference in aerodynamic forces. In contrast, under high turbulence intensity ($I_x = 9\%$), the pressure distribution on the front of the head carriage changes substantially: the pressure on the lower surface increases, while that on the upper surface decreases. Consequently, this configuration generates lower drag and higher lift in this region.

Figure 18 presents the instantaneous surface pressure coefficient distribution on the head carriage for both the Baseline and the high turbulence intensity case ($I_x = 9\%$). The Baseline case exhibits a generally symmetric

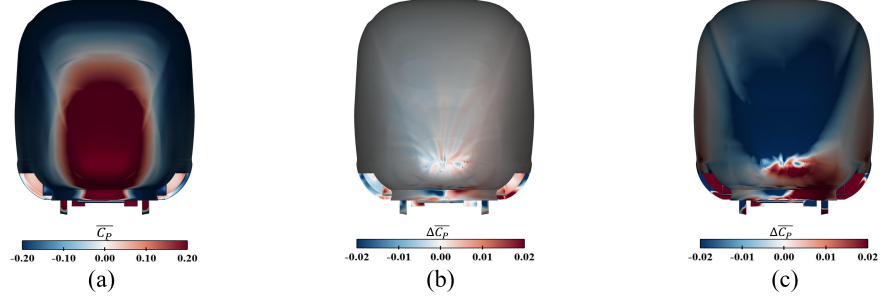


Figure 17: Time-averaged surface pressure coefficient distribution of the front of the head carriage: (a) time-averaged C_P of Baseline; (b) $\Delta C_P(2\%)$; (c) $\Delta C_P(9\%)$.

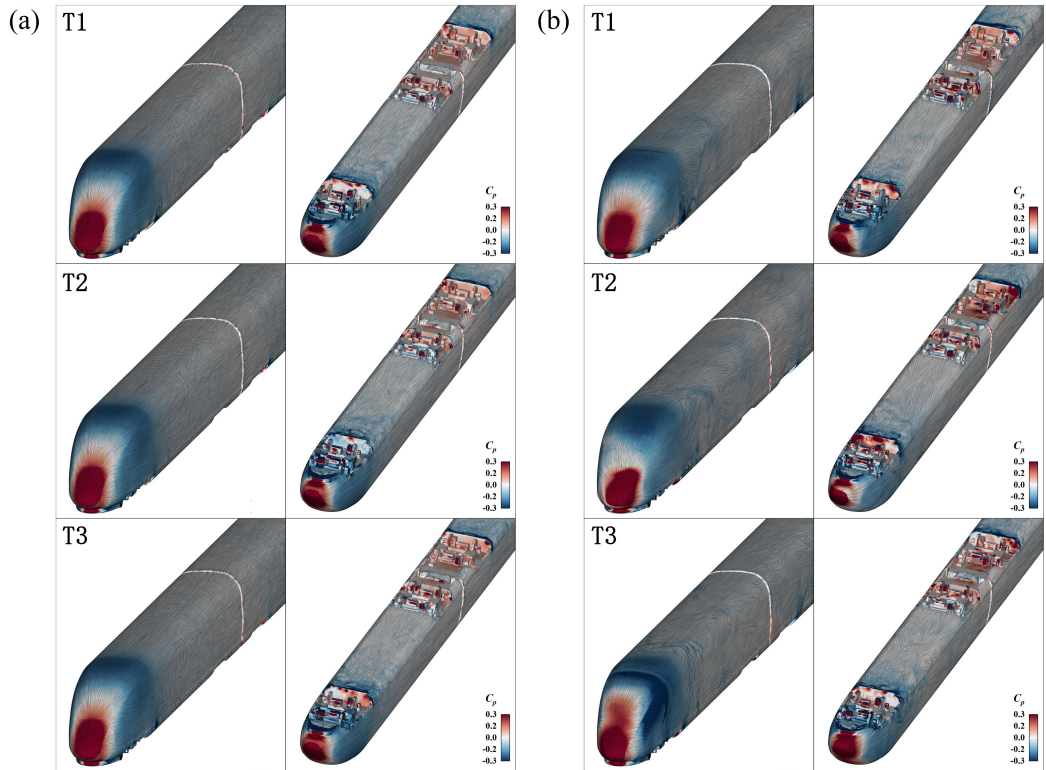


Figure 18: Instantaneous surface pressure coefficient distribution of the front of the head car: (a) Instantaneous C_P of Baseline; (b) Instantaneous C_P of $I_x=9\%$.

528 pressure distribution. However, under high turbulence intensity, the flow field
 529 becomes notably asymmetric, resembling a crosswise effect. This asymmetry
 530 induces the airflow to impact the head of the train at a slight yaw angle, di-

531 minimizing the positive pressure area and thereby reducing the head pressure.
 532 Simultaneously, due to the crosswise effect, the side flow accelerates, leading
 533 to a substantial decrease in side pressure. Additionally, this side pressure
 534 asymmetry allows more flow to enter the bogie cavity, increasing the pres-
 535 sure near its rear edge. From this, it can also be deduced that the alternating
 536 load applied to the carriage increases, which may further harm the operating
 537 smoothness.

538 Figure 19 presents the time-averaged surface pressure coefficient on the
 539 bottom of the train for the Baseline, $I_x = 2\%$, and $I_x = 9\%$. Notably, for
 540 Baseline, in the straight section near the trailing edge of the bogie cavity,
 541 pressure decreases substantially due to flow separation, which in turn reduces
 542 lift, in accordance with the results shown in Figure 13. Additionally, as the
 543 flow velocity decreases in the straight section of the bottom, the pressure
 544 rises to nearly zero before entering the second bogie cavity, leading to an
 545 increase in lift. Under high turbulence ($I_x = 9\%$), the pressure distribution

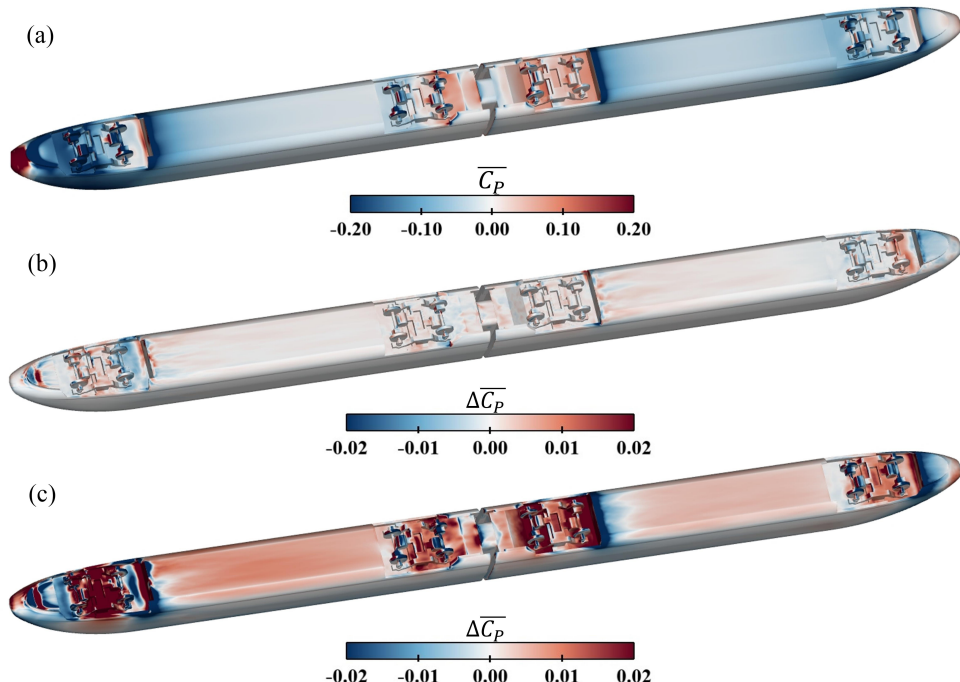


Figure 19: Time-averaged surface pressure coefficient distribution of the bottom of the train: (a) time-averaged C_P of Baseline; (b) $\Delta C_{P(2\%)}$; (c) $\Delta C_{P(9\%)}$.

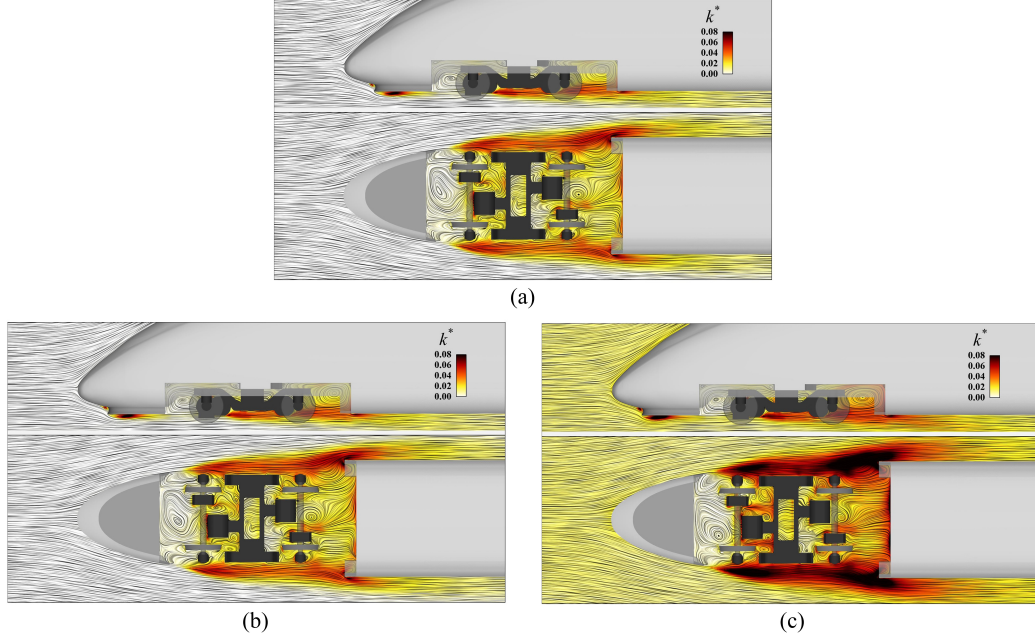


Figure 20: Turbulent kinetic energy distribution in the first bogie region: (a) Baseline; (b) $I_x = 2\%$; (c) $I_x = 9\%$.

on the bottom surface of the straight section is higher than that of Baseline, which could be the reason for the increase of lift force here. The pressure in the four bogie cavities also increases. A comparison of the four bogie cavities reveals that the first one experiences the highest pressure difference $\Delta C_P(9\%)$ among them four. From the results, it is deduced that under high turbulence intensity, lift at the front of the head carriage and in the bottom of the straight section increases significantly. Whereas, for low turbulence intensity, lift remains nearly unchanged compared to the Baseline, $\Delta C_P(2\%)$ is less than 0.002 at most locations. This aligns with the observation that lift increases parabolically with turbulence intensity indicated in Figure 9b.

From the above analyses, it is clear that the influence of the bogie cavity on the aerodynamic forces of the HST is significant. To give a better understanding of the flow in the bogie cavities, Figure 20 shows the turbulent kinetic energy in the first bogie region under different turbulence intensities. As the turbulence intensity increases, the turbulent kinetic energy on both sides of the bogie correspondingly rises. Consequently, the flow mixing phenomenon within the shear layer between the bogie cavity and the underbody

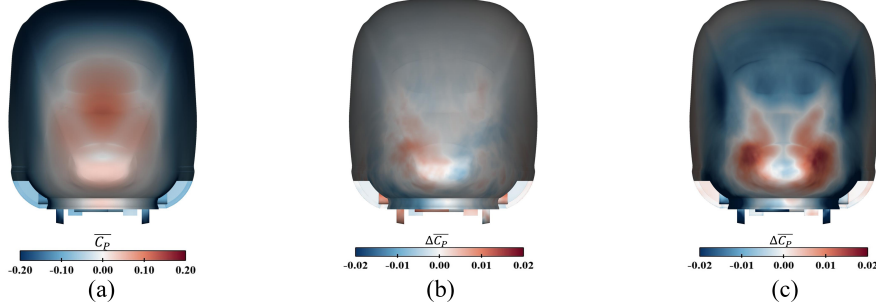


Figure 21: Time-averaged surface pressure coefficient distribution of the rear of the tail carriage: (a) Baseline; (b) $I_x = 2\%$; (c) $I_x = 9\%$.

airflow is intensified, which allows for a greater influx of airflow into the bogie cavity, aligning with the high-pressure region depicted in Figure 19. This variation in turbulent kinetic energy could enhance the interaction at the fluid-solid surface. What's more, the turbulent kinetic energy near the rear surface of the bogie cavity also increases, which could be the reason for the changes in pressure here.

Figure 21 shows the time-averaged surface pressure coefficient distribution of the rear of the tail carriage for the cases of the Baseline, $I_x = 2\%$ and $I_x = 9\%$. For the Baseline, as the airflow enters the curve section, the surface pressure registers as a negative value, subsequently transitioning to a positive value near the tail nose, consistent with the results shown in Figures 5b and 14a. Similarly to the above results, low turbulence intensity has a minimal effect. However, under the conditions of $I_x = 9\%$, the upper surface as well as the upper half of side surfaces induce more negative pressure and increase the pressure drag. An annular high-pressure zone is also generated around the nose edge, potentially indicating specific fluid-structure interactions occurring during the wake formation.

3.2. Turbulence length scale

During the operation of HST, varying turbulence length scales are typically encountered due to diverse terrain and different atmospheric boundary layer conditions. This section examines the influence of turbulence length scale on HST by comparing aerodynamic forces and boundary layer development under different turbulence length scale conditions. The surface pressure distributions are not further investigated as they show very similar trends as varying turbulence intensity.

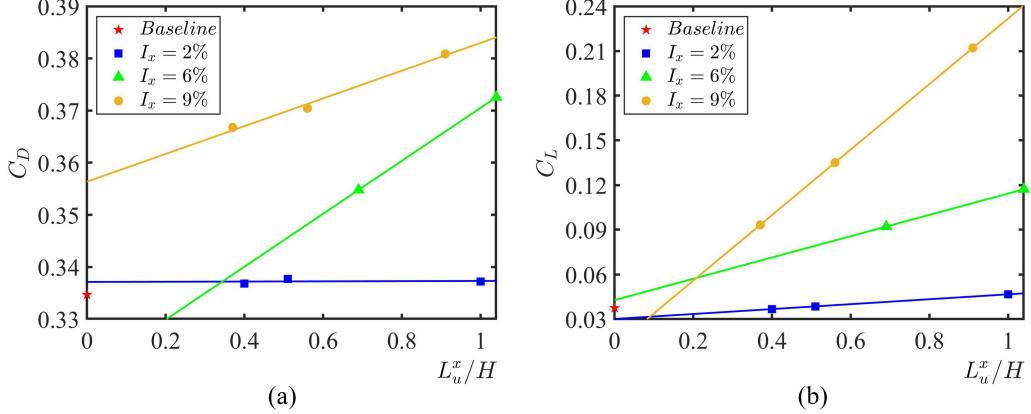


Figure 22: Distribution of time-averaged integral force coefficients with turbulence length scale: (a) drag coefficient (C_D); (b) lift coefficient (C_L).

588 3.2.1. Aerodynamic forces

589 Figure 22 presents the distribution of integral aerodynamic coefficients as
590 a function of turbulence length scale across varying turbulence intensities.
591 As indicated, both drag and lift coefficients increase with an increase in the
592 turbulence length scale, regardless of turbulence intensity. Under low turbu-
593 lence intensity conditions ($I_x = 2\%$, blue curve), the influence of turbulence
594 length scale on drag and lift coefficients is minimal. Therefore, this section
595 focuses exclusively on results under high turbulence intensity, specifically
596 case 8 (Ix09_L056H), case 9 (Ix09_L091H), and case 10 (Ix09_L037H), all of
597 which with a turbulence intensity of 9%.

598 Figure 23 illustrates the relative increase in aerodynamic force coefficients
599 with RMS for the head carriage, tail carriage, and entire train set under
600 various turbulence length scale conditions compared to the Baseline. From
601 the results of an individual carriage or the entire train set, turbulence length
602 scale affects the drag and lift forces on the head carriage, tail carriage, and
603 entire train set in a similar way to that of changing the turbulence intensity.
604 The drag and lift as well as their fluctuations increase when encountering
605 larger turbulence length scales.

606 However, when analyzing specific decomposed components (Figure 24),
607 where the carriages are further divided into bodies, bogies, and bogie cav-
608 ities, the influence of turbulence length scale diverges notably from that of
609 turbulence intensity. Specifically, the drag on the head body decreases mono-
610 tonically as the turbulence length scale increases, however, the drag on the

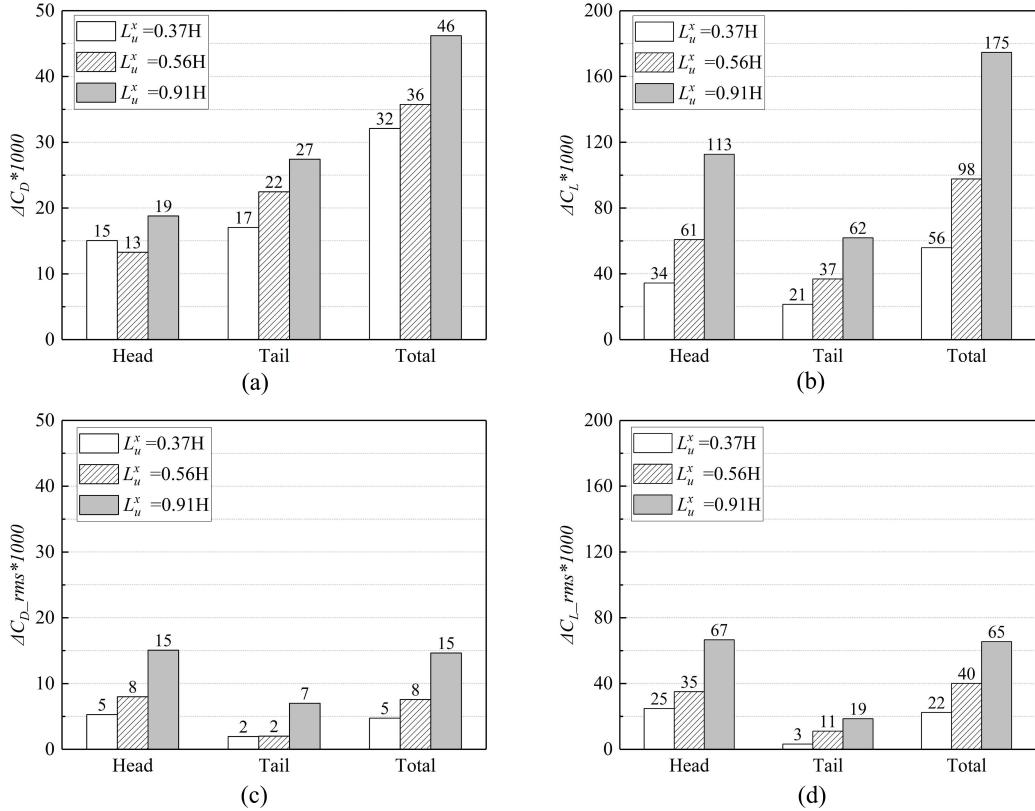


Figure 23: The increment of aerodynamic force coefficients of the two carriages at $I_x = 9\%$:
(a) time-averaged C_D ; (b) time-averaged C_L ; (c) RMS of C_D ; (d) RMS of C_L .

tail body changes little. In terms of lift, as well as RMS of both drag and lift, the trends are very similar compared to the varying turbulence intensity. In other words, the impact of longer turbulence length scales on aerodynamic forces is essentially equivalent to a higher turbulence intensity.

To clarify the reasons for the differences in drag, curves of decomposed cumulative drag coefficients along the flow direction are plotted in Figure 25. The influence of pressure drag are similar to the trend observed as turbulence intensity increases. As the turbulence length scale grows, the pressure drag on the curve section of the head body decreases. However, the viscous drag of the head body decreases with the turbulence length scale, contrary to the influence of turbulence intensity. Therefore, for the head carriage, both pressure drag in the curve section with bogie structures and viscous drag in the straight section decrease along with the increase of turbulence

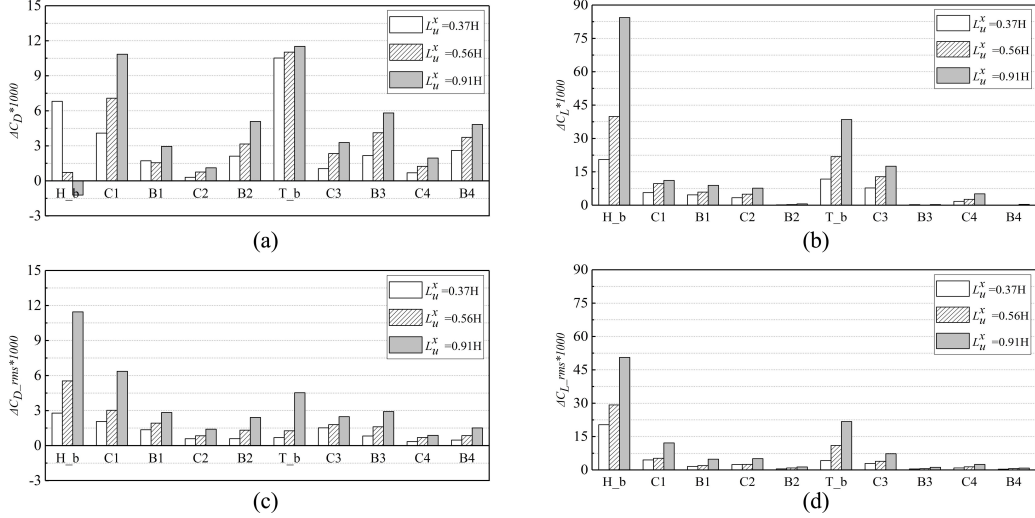


Figure 24: The increment of aerodynamic force coefficients of train components at $I_x = 9\%$ under different turbulence length scales: (a) time-averaged C_D ; (b) time-averaged C_L ; (c) RMS of C_D ; (d) RMS of C_L . The definitions of abbreviations are the same in Figure 11.

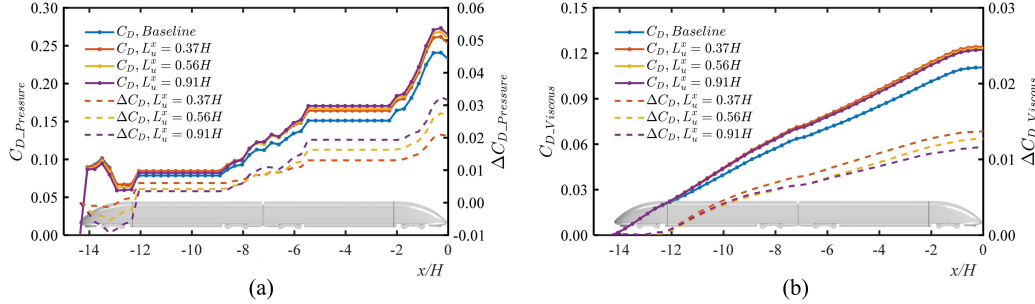


Figure 25: Decomposed cumulative drag coefficients along the flow direction at high turbulence intensity ($I_x \approx 9\%$): (a) pressure drag $C_{D,\text{Pressure}}$; (b) viscous drag $C_{D,\text{Viscous}}$.

length scale. Finally, the drag exerted on the head carriage with increasing turbulence length scale exhibits a reduction trend.

3.2.2. Boundary layer

Figure 26 shows the displacement thickness δ_1 and moment thickness δ_2 distributing along the longitudinal symmetry line at the top of the train under different turbulence length scales. The influence of turbulence length scale is not obvious from the three cases with turbulence configurations. Furthermore, a comparison among these three cases reveals that the boundary layer

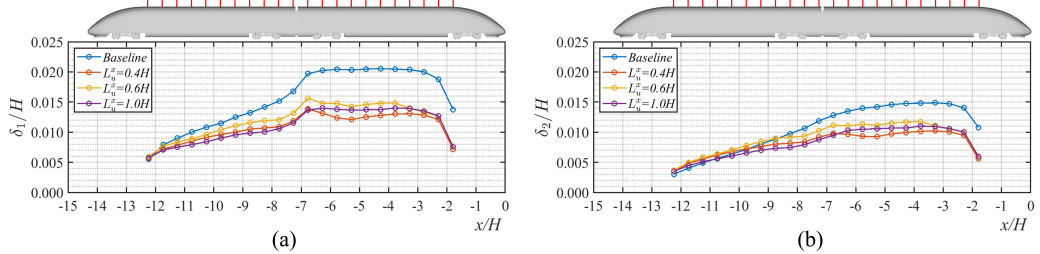


Figure 26: Displacement thickness and moment thickness distributions along the longitudinal symmetry line at the top of the train under varying turbulence length scale: (a) displacement thickness δ_1 ; (b) moment thickness δ_2 .

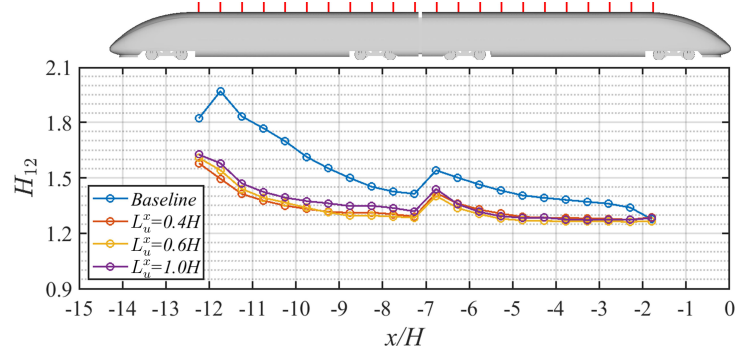


Figure 27: Shape factor H_{12} distributions along the longitudinal symmetry line at the top of the train under varying turbulence length scale.

thickness for the $L_u^x = 0.6H$ configuration remains consistently the greatest. In the other two configurations, the boundary layer thickness in the head carriage is greater for $L_u^x = 0.4H$ than for $L_u^x = 1.0H$, while the opposite result is observed in the tail carriage. This transitional process occurs in the carriage junction region, which may be associated with changes in the turbulence state of the boundary layer. From Figure 27, it is shown that the shape factors H_{12} distributed on the tail carriage for the three turbulence cases are basically the same. However, for $L_u^x = 1.0H$, the shape factor is higher than the other two cases on the head carriage. This could be attributed to the fact that, under the same turbulence intensity, an incoming flow with a larger turbulence length scale contains less energy in small-sized eddies, which contributes to the momentum within the initial boundary layer. Thus, the significance of the design of carriage junction is once again substantiated.

645 **4. Conclusions**

646 In this paper, an IDDES simulation combined with the STG method
647 is used to investigate the effects of incoming turbulence on the aerodynamic
648 characteristics of a 1/18 scale two-carriage HST. Ten configurations of incom-
649 ing turbulence, each with different turbulence intensities and length scales,
650 are simulated and analyzed. As the first part of this series of technical pa-
651 pers, aerodynamic forces, boundary layers, and pressure distributions are
652 comprehensively examined, considering the two turbulence properties. The
653 main conclusions are as follows.

- 654 1. With the increase of either turbulence intensity or turbulence length scale,
655 the mean drag and lift coefficient of the train both increase, with the
656 maximum increase up to 46 counts and 175 counts, respectively, obtained
657 at when turbulence intensity is 9% and length scale is 0.91H.
- 658 2. The incoming turbulence acts on the carriage similarly to a crosswind,
659 weakening the impact on the head carriage and reducing surface pressure,
660 which results in drag reduction and lift increase. Additionally, the flow
661 around the curve section of the tail carriage accelerates, further decreas-
662 ing surface pressure and thereby increasing the pressure drag on the tail
663 carriage.
- 664 3. Incoming turbulence increases the turbulent kinetic energy within the
665 shear layers beside the bogie cavity, intensifying the mixing between the
666 underbody flow and the flow within the cavity. This allows more flow to
667 tend to enter the cavity, thereby increasing drag. The intensified interac-
668 tion between the flow and the bogie cavity reduces the underbody velocity
669 and raises the surface pressure, thereby increasing lift on the straight sec-
670 tion.
- 671 4. The high turbulence intensity of the incoming flow decreases the shape
672 factor of the boundary layer on the body surface, which increases the
673 velocity gradient and the viscous drag. Larger turbulence length scale
674 increases the shape factor.
- 675 5. The design of the carriage junction is crucial to the aerodynamic forces
676 by introducing significant changes to the flow state in the boundary layer.

677 **Declarations**

678 **• Funding:**

679 This work was supported by the National Natural Science Foundation of

680 China (Grand No. 51905381), Shanghai Key Laboratory of Aerodynamics
681 and Thermal Environment Simulation for Ground Vehicles (Grant No.
682 23DZ2229029) and the National Natural Science Foundation of China (Grant
683 No. 51875411).

684 **• Conflicts of interest:**

685 The authors have no conflicts of interest to declare that are relevant to the
686 content of this article.

687 **• Data availability:**

688 Data will be made available on request.

689 **References**

- 690 [1] J. R. Bell, D. Burton, M. Thompson, A. Herbst, J. Sheridan, Wind
691 tunnel analysis of the slipstream and wake of a high-speed train, *Journal*
692 of Wind Engineering and Industrial Aerodynamics 134 (2014) 122–138.
- 693 [2] J. R. Bell, D. Burton, M. Thompson, A. Herbst, J. Sheridan, A wind-
694 tunnel methodology for assessing the slipstream of high-speed trains,
695 *Journal of Wind Engineering and Industrial Aerodynamics* 166 (2017)
696 1–19.
- 697 [3] J. R. Bell, D. Burton, M. Thompson, A. Herbst, J. Sheridan, Moving
698 model analysis of the slipstream and wake of a high-speed train, *Journal*
699 of Wind Engineering and Industrial Aerodynamics 136 (2015) 127–137.
- 700 [4] L. Zhang, M. Z. Yang, J. Q. Niu, X. F. Liang, J. Zhang, Moving model
701 tests on transient pressure and micro-pressure wave distribution induced
702 by train passing through tunnel, *Journal of Wind Engineering and*
703 *Industrial Aerodynamics* 191 (2019) 1–21.
- 704 [5] C. Xia, X. Shan, Z. Yang, Detached-eddy simulation of ground effect
705 on the wake of a high-speed train, *Journal of Fluids Engineering* 139
706 (2017a).
- 707 [6] S. B. Wang, D. Burton, A. Herbst, J. Sheridan, M. C. Thompson, The
708 effect of bogies on high-speed train slipstream and wake, *Journal of*
709 *Wind Engineering and Industrial Aerodynamics* 83 (2018) 471–489.
- 710 [7] G. Chen, X. Li, L. Zhang, X. Liang, S. Meng, D. Zhou, Numerical
711 analysis of the effect of train length on train aerodynamic performance,
712 *AIP Advances* 12 (2022) 025201.
- 713 [8] M. Yu, R. Jiang, Q. Zhang, et al., Crosswind stability evaluation of high-
714 speed train using different wind models, *Chinese Journal of Mechanical*
715 *Engineering* 32 (2019) 40.
- 716 [9] S. Wordley, J. Saunders, On-road turbulence, *SAE International Journal*
717 of Passenger Cars-Mechanical Systems 1 (2008) 341–360.
- 718 [10] H. Gao, T. Liu, X. Chen, H. Zeng, J. Jiang, X. Wang, B. C. Khoo,
719 Turbulence correlation between moving trains and anemometer tow-
720 ers: Theoretical analysis, field measurements and simulation, *Journal*

- 721 of Wind Engineering and Industrial Aerodynamics 255 (2024) 105949.
722 doi:10.1016/j.jweia.2024.105949.
- 723 [11] B. E. Lee, Some effects of turbulence scale on the mean forces on a
724 bluff body, Journal of Wind Engineering and Industrial Aerodynamics
725 1 (1975) 361–370.
- 726 [12] P. W. Bearman, T. Morel, Effect of free stream turbulence on the flow
727 around bluff bodies, Progress in Aerospace Sciences 20 (1983) 97–123.
- 728 [13] C. Zhao, H. Wang, L. Zeng, M. M. Alam, X. Zhao, Effects of oncoming
729 flow turbulence on the near wake and forces of a 3d square cylinder,
730 Journal of Wind Engineering and Industrial Aerodynamics 168 (2021)
731 177–189.
- 732 [14] M. Li, Q. Li, H. Shi, M. Li, Effects of free-stream turbulence on the
733 near wake flow and aerodynamic forces of a square cylinder, Journal of
734 Fluids and Structures 114 (2022) 103748.
- 735 [15] D. Burton, S. Wang, D. T. Smith, H. N. Scott, T. N. Crouch, M. C.
736 Thompson, The influence of background turbulence on ahmed-body
737 wake bistability, Journal of Fluid Mechanics 926 (2021).
- 738 [16] D. Schröck, N. Widdecke, J. Wiedemann, The effect of high turbulence
739 intensities on surface pressure fluctuations and wake structures of a ve-
740 hicle model, SAE International Journal of Passenger Cars-Mechanical
741 Systems 2 (2009) 98–110.
- 742 [17] R. Hearst, G. Gomit, B. Ganapathisubramani, Effect of turbulence on
743 the wake of a wall-mounted cube, Journal of Fluid Mechanics 804 (2016)
744 513–530.
- 745 [18] R. Blumrich, N. Widdecke, J. Wiedemann, A. Michelbach, F. Wittmeier,
746 O. Beland, New fkfs technology at the full-scale aeroacoustic wind tunnel
747 of university of stuttgart, SAE International Journal of Passenger Cars
748 - Mechanical Systems 8 (2015) 294–305.
- 749 [19] X. Fei, T. Kuthada, A. Wagner, J. Wiedemann, The effect of unsteady
750 incident flow on drag measurements for different vehicle geometries in
751 an open jet wind tunnel, SAE International Journal of Advances and
752 Current Practices in Mobility 4 (2022) 1999–2011.

- 753 [20] B. McAuliffe, A. Wall, G. Larose, Simulation of atmospheric turbulence
754 for wind-tunnel tests on full-scale light-duty vehicles, SAE International
755 Journal of Passenger Cars-Mechanical Systems 9 (2016a) 583–591.
- 756 [21] B. McAuliffe, A. D'Auteuil, A system for simulating road-representative
757 atmospheric turbulence for ground vehicles in a large wind tunnel, SAE
758 International Journal of Passenger Cars-Mechanical Systems 9 (2016b)
759 817–830.
- 760 [22] G. Chen, X. B. Li, X. F. Liang, Iddes simulation of the performance
761 and wake dynamics of the wind turbines under different turbulent inflow
762 conditions, Energy 238 (2022) 121772.
- 763 [23] N. Jarrin, S. Benhamadouche, D. Laurence, R. Prosser, A synthetic-
764 eddy-method for generating inflow conditions for large-eddy simulations,
765 International Journal of Heat and Fluid Flow 27 (2006) 585–593.
- 766 [24] Q. S. Li, G. Hu, B. W. Yan, Investigation of the effects of free-stream
767 turbulence on wind-induced responses of tall building by large eddy
768 simulation, Wind & Structures 18 (2014) 599–618.
- 769 [25] M. L. Shur, P. R. Spalart, M. K. Strelets, A. K. Travin, Synthetic
770 turbulence generators for RANS-LES interfaces in zonal simulations of
771 aerodynamic and aeroacoustic problems, Flow, Turbulence and Com-
772 bustion 93 (2014) 63–92.
- 773 [26] D. Stoll, J. Wiedemann, Active crosswind generation and its effect on
774 the unsteady aerodynamic vehicle properties determined in an open jet
775 wind tunnel, SAE International Journal of Passenger Cars - Mechanical
776 Systems 11 (2018) 429–446.
- 777 [27] X. Fei, C. Jessing, T. Kuthada, J. Wiedemann, A. Wagner, The influence
778 of different unsteady incident flow environments on drag measurements
779 in an open jet wind tunnel, Fluids 5 (2020) 178.
- 780 [28] D. Stoll, C. Schoenleber, F. Wittmeier, T. Kuthada, J. Wiedemann,
781 Investigation of aerodynamic drag in turbulent flow conditions, SAE
782 International Journal of Passenger Cars - Mechanical Systems 9 (2016)
783 733–742.

- 784 [29] A. P. Gaylard, N. Oettle, J. Gargoloff, B. Duncan, Evaluation of non-
785 uniform upstream flow effects on vehicle aerodynamics, SAE International
786 Journal of Passenger Cars-Mechanical Systems 7 (2014) 692–702.
- 787 [30] B. Duncan, L. D'Alessio, J. Gargoloff, A. Alajbegovic, Vehicle aerody-
788 namics impact of on-road turbulence, Proceedings of the Institution of
789 Mechanical Engineers, Part D: Journal of Automobile Engineering 231
790 (2017) 1148–1159.
- 791 [31] W. Yang, Y. Liu, E. Deng, X. He, M. Lei, Y. Zou, Comparative study on
792 the wind characteristics of tunnel–bridge and tunnel–flat ground infras-
793 tructures on high-speed railway, Journal of Wind Engineering and In-
794 dustrial Aerodynamics 226 (2022) 105006. doi:10.1016/j.jweia.2022.
795 105006.
- 796 [32] M. Wu, Y. Li, X. Chen, P. Hu, Wind spectrum and correlation char-
797 acteristics relative to vehicles moving through cross wind field, Journal
798 of Wind Engineering and Industrial Aerodynamics 133 (2014) 92–100.
799 doi:10.1016/j.jweia.2014.08.004.
- 800 [33] A. Cogotti, Update on the pininfarina “turbulence generation system”
801 and its effects on the car aerodynamics and aeroacoustics, in: SAE 2004
802 World Congress & Exhibition, 2004-01-0807, 2003.
- 803 [34] D. Stoll, C. Schoenleber, F. Wittmeier, T. Kuthada, J. Wiedemann,
804 Investigation of aerodynamic drag in turbulent flow conditions, SAE
805 International Journal of Passenger Cars-Mechanical Systems 9 (2016)
806 733–743.
- 807 [35] C. J. Baker, C. G. Robinson, The assessment of wind tunnel testing
808 techniques for ground vehicles in cross winds, Journal of Wind Engi-
809 neering and Industrial Aerodynamics 33 (1990) 429–438.
- 810 [36] M. Boccilone, F. Cheli, R. Corradi, S. Muggiasca, G. Tomasini, Cross-
811 wind action on rail vehicles: Wind tunnel experimental analyses, Journal
812 of Wind Engineering and Industrial Aerodynamics 96 (2008) 584–610.
- 813 [37] F. Cheli, S. Giappino, L. Rosa, G. Tomasini, M. Villani, Experimen-
814 tal study on the aerodynamic forces on railway vehicles in presence of
815 turbulence, Journal of Wind Engineering and Industrial Aerodynamics
816 123 (2013) 311–316.

- 817 [38] H. Gao, T. Liu, H. Gu, Z. Jiang, X. Huo, Y. Xia, Z. Chen, Full-scale
818 tests of unsteady aerodynamic loads and pressure distribution on fast
819 trains in crosswinds, *Measurement* 186 (2021) 110152.
- 820 [39] W. Yang, H. Yue, E. Deng, Y. Wang, X. He, Y. Zou, Influence of
821 the turbulence conditions of crosswind on the aerodynamic responses
822 of the train when running at tunnel-bridge-tunnel, *Journal of Wind*
823 *Engineering and Industrial Aerodynamics* 229 (2022) 105138.
- 824 [40] C. G. Robinson, C. J. Baker, The effect of atmospheric turbulence on
825 trains, *Journal of Wind Engineering and Industrial Aerodynamics* 34
826 (1990) 251–272.
- 827 [41] E. Deng, H. Yue, Y.-Q. Ni, Y.-W. Wang, X.-H. He, Z.-W. Chen, A
828 turbulent crosswind simulation method at high-speed railway tunnel en-
829 trance: Based on field test and geometric turbulence generator, *Physics*
830 *of Fluids* 35 (2023) 015156. doi:10.1063/5.0133292.
- 831 [42] H. Yue, J. Wang, E. Deng, Y.-Q. Ni, W.-C. Yang, X.-Y. Liu, C.-M.
832 Tsang, How do crosswinds from two turbulent generators affect the
833 aerodynamic loads of running trains at tunnel entrances?, *Physics of*
834 *Fluids* 35 (2023) 125137. doi:10.1063/5.0177331.
- 835 [43] J. Q. Niu, D. Zhou, X. F. Liang, Experimental research on the aero-
836 dynamic characteristics of a high-speed train under different turbulence
837 conditions, *Experimental Thermal and Fluid Science* 80 (2017) 117–125.
- 838 [44] R.-D. Xue, X.-H. Xiong, X.-B. Li, G. Chen, Influence of turbulent in-
839 coming flow on aerodynamic behaviors of train at 90° yaw angle, *Physics*
840 *of Fluids* 35 (2023) 015121. doi:10.1063/5.0135930.
- 841 [45] R.-D. Xue, X.-H. Xiong, G. Chen, Flow dynamics of train under tur-
842 bulent inflow at different crosswind yaw angles, *Physics of Fluids* 36
843 (2024) 035176. doi:10.1063/5.0195426.
- 844 [46] J. García, J. Muñoz-Paniagua, A. Crespo, Numerical study of the aero-
845 dynamics of a full scale train under turbulent wind conditions, including
846 surface roughness effects, *Journal of Fluids and Structures* 74 (2017) 1–
847 18. doi:doi.org/10.1016/j.jfluidstructs.2017.07.007.

- 848 [47] J. García, J. Muñoz-Paniagua, A. Jiménez, E. Migoya, A. Crespo, Numerical study of the influence of synthetic turbulent inflow conditions on
849 the aerodynamics of a train, *Journal of Fluids and Structures* 56 (2015)
850 134–151. doi:doi.org/10.1016/j.jfluidstructs.2015.05.002.
- 852 [48] European Union Agency for Railways, Technical Specifications for
853 Interoperability (TSIs), 2024. URL: www.era.europa.eu/domains/technical-specifications-interoperability_en, accessed: 2024-
854 10-23.
- 856 [49] M. L. Shur, P. R. Spalart, M. K. Strelets, A. K. Travin, A hybrid RANS-LES
857 approach with delayed-DES and wall-modelled LES capabilities,
858 *International Journal of Heat and Fluid Flow* 29 (2008) 1638–1649.
- 859 [50] C. Xia, H. F. Wang, X. Z. Shan, Z. G. Yang, Q. L. Li, Effects of ground
860 configurations on the slipstream and near wake of a high-speed train,
861 *Journal of Wind Engineering and Industrial Aerodynamics* 168 (2017b)
862 177–189.
- 863 [51] Z. Zhou, C. Xia, X. Shan, Z. Yang, The impact of bogie sections on the
864 wake dynamics of a high-speed train, *Flow, Turbulence and Combustion*
865 104 (2019) 89 – 113.
- 866 [52] J. Saunders, S. Wordley, A review of measurement of ambient turbulence
867 with respect to ground vehicles, in: *SAE 2006 Transactions Journal of*
868 *Passenger Cars: Mechanical Systems*, 2006-01-1028, 2006.
- 869 [53] P. L. O'Neill, D. Nicolaides, D. Honnery, J. Soria, Autocorrelation functions
870 and the determination of integral length with reference to experimental
871 and numerical data, in: *15th Australasian fluid mechanics conference*, volume 1,
872 University of Sydney, Sydney, NSW, Australia, 2004,
873 pp. 1–4.
- 874 [54] E. E. Morfiadakis, G. L. Glinou, M. J. Koulouvari, The suitability of the
875 von karman spectrum for the structure of turbulence in a complex terrain
876 wind farm, *Journal of Wind Engineering and Industrial Aerodynamics*
877 62 (1996) 237–257.